Osaka University Knowledge Archive

Title	Crossed-Beam Experiment onf Rotational Population Distribution of OH(A 2Σ+) Split from H2O by Lyman Alpha Photon Impact
Author(s)	山下, 巌
Citation	大阪大学, 1975, 博士論文
Version Type	VoR
URL	https://hdl.handle.net/11094/267
rights	
Note	

Osaka University Knowledge Archive : OUKA

https://ir.library.osaka-u.ac.jp/

Osaka University

DISSERTATION IN PHYSICS

CROSSED-BEAM EXPERIMENT ON ROTATIONAL POPULATION DISTRIBUTION OF $OH(A\ ^2\Sigma^+)$ SPLIT FROM H_2O BY LYMAN ALPHA PHOTON IMPACT

by

Iwao YAMASHITA

THE OSAKA UNIVERSITY

GRADUATE SCHOOL OF SCIENCE

TOYONAKA, OSAKA

CROSSED-BEAM EXPERIMENT ON ROTATIONAL POPULATION DISTRIBUTION OF OH ($A\ ^2\Sigma^+$) SPLIT FROM H_2O BY LYMAN ALPHA PHOTON IMPACT

by

Iwao YAMASHITA

Submitted to Graduate School of Science in Partial Fulfilment
of the Requirements for the Degree of
Doctor of Science
OSAKA UNIVERSITY
1975

CONTENTS

Abstract ---------- 1

PART I. Highly Monochromatic Lyman Alpha Light Source of Plasma-Jet Type

(l) Introduction ---------- 3

(2) Apparatus ---------- 4

(3) Experiments ---------- 6

(4) Emission Mechanism ---------- 9

(5) Comparison with Microwave-Powered Sources ----- 15

(6) Conclusion ---------- 16

PART II. Crossed-Beam Experiment on Rotational Population Distribution of OH($A\ ^2\Sigma^+$) Split from H_2O by Lyman Alpha Photon Impact

(1) Introduction ---------- 29

(2) Crossed-Beam Apparatus ---------- 32

(3) Experimental Results ---------- 35

(4) Theoretical Interpretation ---------- 37

(5) Comparison with Target-Gas Experiments -------- 40

(6) Conclusion ---------- 44

APPENDIX A. Predissociation in OH ($A\ ^2\Sigma^+$) ---------- 63

APPENDIX B. Correlation Diagrams for Electronic States of H_2O and Potential Energy Surface of the $\widetilde{B}\ ^1A_1$ State

(1) Excited States of H_2O ---------- 73

(2) Correlation Diagrams ---------- 73

(3) Potential Energy Surface of the $\widetilde{B}\ ^1A_1$ State -- 75

Acknowledgements ---------- 91

Abstract

In Part I, a highly monochromatic light source of the hydrogen Lyman α line λ 1216 has been developed by means of the technique of an expanded argon plasma-jet admixed with hydrogen. This light source is completely monochromatic, as far as the wavelength range from λ 1530 to 1050 is concerned. Moreover, the intensity of the Lyman α beam through a LiF window and a light guide is 2×10^{15} quanta/cm^{2}s at the distance 10 cm from the LiF window. These properties are superior to those obtained by the conventional microwave-powered light source. The simple structure of the spectrum and the intense emission of Lyman α from the present light source have been discussed on the basis of the second-kind collisions of the metastable argon with the atomic and molecular hydrogen.

In Part II, the initial rotational population distribution of OH($A\ ^2\Sigma^+$) produced by Lyman α photon impact on H_2O has been measured by the crossed-beam technique. The light source employed is of the plasma-jet type mentioned above, and it is highly monochromatic. The result obtained tells that the population is negligibly small in the lower rotational levels, and the overall distribution curve looks like an asymmetric peak with a narrow half–width situated at K'=17 to 22.

Measurements have also been made in the target-gas method. However, these results are sensitive to the pressure of the target gas

in the fluorescence cell, and they are all different more or less from the result obtained by the crossed-beam technique. Discussions about the discrepancy have led to secondary productions of OH($A\ ^2\Sigma^+$) due to long-lived species such as OH ($X\ ^2\Pi$), O(^1D) and H(^2S) because of their at-random motions in the target gas.

PART I

HIGHLY MONOCHROMATIC LYMAN ALPHA LIGHT SOURCE OF PLASMA-JET TYPE

(1) Introduction

For spectroscopic studies on inelastic photon-molecule collisions, it is required for one to have intense monochromatic light sources in the vacuum ultraviolet region. For instance, the hydrogen resonance line λ 1216 is one of the most important solar emission lines and plays an important role in the photon-molecule collisions in the upper atmosphere and space.

The requirement for high intensity is dictated by the necessities for detection and for high resolution spectroscopy of very weak light signals emitted by collision products. The requirement for purely monochromatic light is necessary to define the excitation energy in photon-molecule collision processes.

The usual way to get monochromatic light is to use a monochromator in conjunction with a strong continuous light source. However, the monochromator is impossible to offer enough intensity, except when the continuum is especially strong, for instance, from SOR (Synchrotron Orbital Radiation). Filters for use in the vacuum ultraviolet have not yet been well developed to satisfy the requirement for single wavelength.

In 1962, Brewer and McGregor [1)] have found that the emission is predominantly due to the hydrogen Balmer series when a small amount of hydrogen is added to an expanded argon plasma-jet at 0.5 Torr. Such an intense emission of the Balmer series leads to an expectation that the plasma-jet may be able to give an intense light source of the hydrogen Lyman series in the vacuum ultraviolet.

The present author has made an attempt to utilize the expanded plasma-jet admixed with hydrogen for an intense monochromatic light source of Lyman α λ 1216. The purposes of the present work are as follows; (1) to design an intense monochromatic light source of Lyman α by means of the technique of an expanded plasma-jet, (2) to study the spectral characteristics of the source, and (3) to make clear the emission mechanisms of the source.

(2) Apparatus

The light source apparatus designed for use in the present work consists of a plasma-jet torch, a light source chamber and an exhausting system, as schematically shown in Fig.1. Argon gas passes through the torch in which an arc is sustained between a tungsten rod (the cathode) and a water-cooled copper nozzle (the anode). The luminous argon plasma thus produced is expanded through the nozzle into the light source chamber. The source chamber is evacuated steadily by an oil rotary pump with an exhausting speed of 3000 l/min.

Hydrogen is injected from four ports at the position of the nozzle exit and diffuses into the expanded plasma-jet. The source chamber is made of stainless-steel and cooled by running water through a copper pipe which is coiled around the chamber. The source chamber has two windows of a diameter 12 mm; a LiF window of thickness 1.5 mm and a glass window, at 48 mm downstream from the nozzle exit. Transmittance of the LiF window decreases gradually during operation of the light source. The original transmittance can be restored by annealing the LiF crystal in the atmosphere of argon at 500 °C for two hours [2,3].
The emission spectrum in the vacuum ultraviolet is taken with a 50 cm radius Seya-Namioka type monochromator. The detector is a sodium salicylate-coated photomultiplier (HTV 1P21). The grating has 600 grooves/mm with a ruled area 51×30 mm^2 and is blazed at 1500 Å. The reciprocal linear dispersion is 33 Å/mm. A slit-width of 40 μm is used. For the visible spectrum, a 30 cm glass-prism monochromator is used with a photomultiplier (HTV R136). The H_α line λ6563 is also measured with an interference filter of half-width 30 Å. The pressure of the gas is measured by a swirl-type McLeod gauge. The gas flow rates of argon and hydrogen are measured by float-type flow meters.

Absolute intensity measurements of the light source have been made with a thermal detector similar to the Coblentz radiometer [4,5]. A flux of the monochromatic light coming out of the LiF window is condensed by a light guide on the front surface of the detector, as shown in Fig.1. The light guide is a truncated pyramid in shape, where the

entrance area is 20×20 mm^2, the exit area 10×10 mm^2, the length 65 mm, and inner surface is evaporated with aluminium and coated with MgF_2. The front surface of the detector is 11×7 mm^2 in area and coated with a carbon thin film of which resistance is 25 kΩ.

As will soon be seen in the next section, the present light source exhibits no other emission than Lyman α below λ 1530. The thermal detector employed may absorb the Lyman α light perfectly. The CH_4 gas absorbs any radiation below λ 1500, too [6]. Then, the intensity of Lyman α from the present source can be determined by comparing the radiant energies recieved by the detector with and without introducing CH_4 gas into the observation chamber. The partial pressure of CH_4 can be measured with the vacuum ultraviolet monochromator [6]. The observation chamber is always filled up with helium at 3 Torr, so that the thermal condition of the detector is not affected by CH_4 introduced.

(3) Experiments

As shown in Fig.2, the visible spectrum of the expanded plasma-jet is changed drastically by adding hydrogen. With increase in hydrogen flow rate Q_{H2}, the Ar I lines are quenched and the hydrogen Balmer series become dominant in the spectrum. At the same time, the expanded plasma-jet changes in color from pink to scarlet.

On the other hand, it is well-known that a large amount of metastable argon is contained in the expanded plasma-jet and the emission of Ar I lines arises predominantly as a result of collisional excitation of metastable argon by electron [1,7–9]. Therefore, Fig.2 suggests that the second-kind collision of metastable argon with admixed hydrogen results in the emission of the Balmer series.

Absorption of Ar I line λ 6965 by metastable argon can be measured with increasing Q_{H2}. For that, a capillary discharge lamp of argon is used as an external source [10–13]. Unfortunately, the measured fractional absorption gives no more than the qualitative measure of the metastable argon density, for lack of the knowledge about the line profile. The experimental result is shown in comparison with the emission intensities of Ar I and H_α, in Fig.3.

Variations of the line intensities of Ar I λ 4159, H_α and Lyman α with Q_{H2} are shown for different argon flow rates Q_{Ar}, in Fig.4. The intensity of Ar I decreases exponentially with increase in Q_{H2}. Since the metastable argon density $[Ar^m]$ is proportional to the intensity of Ar I, the following equation holds,

$$[Ar^m] = [Ar^m]_0 \exp(-\alpha Q_{H2}), \quad (1)$$

where $[Ar^m]_0$ denotes the metastable argon density at $Q_{H2} = 0$. The parameter α becomes smaller with increase in Q_{Ar}. It may be the reason why α depends on Q_{Ar} that diffusion of hydrogen slows down with increase in Q_{Ar}.

Supposing the hydrogen atom is excited by the second-kind collision as mentioned above, then the intensities of both H_α and Lyman α may be proportional to the product [H][Ar^m], where [H] denotes the atomic hydrogen density. It may be confirmed qualitatively in Fig.4, since [H] may increase linearly with increasing Q_{H2}.

Moreover, the intensities of Lyman α and H_α depend on Q_{H2} in somewhat different ways in Fig.4. Such a difference can be seen more clearly in the dependence of these intensities upon the arc current of the torch, as shown in Fig.5. The intensity of Lyman α is approximately in proportion to the square root of the arc current. On the other hand, the intensity of H_α increases linearly with the arc current. This difference may be due to the self-absorption effect of Lyman α, because the Lyman α resonance line is highly absorbed by the hydrogen atom in the ground state. It may be expected that dissociation of admixed hydrogen becomes more efficient with increase in the input power of the plasma-jet torch.

The optimum conditions for operation of the expanded plasma-jet as the intense monochromatic source of Lyman α can be determined on the basis of the preceding results. In that case, stable operation of the source must also be considered. The best conditions are as follows: arc current 200 A, arc voltage 20 V, arc input power 4 kW, Q_{Ar} 15 l/min, Q_{H2} 0.5 l/min and source chamber pressure 4.5 Torr.

The vacuum ultraviolet spectrum obtained under these conditions is shown in Fig.6. The radiation shorter than λ 1050 is absorbed by the LiF window. The intense emission of Lyman α and the weak emission around λ1600 are observed. The latter emission is attributed in part to the Lyman bands of H_2 [14]. It is found that the intensity of the background continuous emission around the Lyman α line is negligible and no impurity lines exist. Therefore, this Lyman α source is completely monochromatic, as far as the wavelength range from λ1530 to 1050 is concerned.

The conventional method for absolute intensity measurements of Lyman α makes use of photoionization of NO [15]. However, in the present work the radiant energy through the light guide is measured by means of the thermal detector. Typically, a total radiant energy is 4.5 mW in the absence of CH_4, while a radiant energy absorbed by CH_4 at 0.17 Torr is 1.3 mW. These data lead to the following radiant energy or intensity of the Lyman α beam at the distance 10 cm from the LiF window; 3 mW/cm^2 or 2×10^{15} quanta/cm^{2}s.

(4) Emission Mechanisms

It is well-known that some atoms and molecules are selectively excited by the second-kind collision with metastable atoms [9–11,16–18]. In the present light source, hydrogen atoms are expected to be excited in the

same way, because the metastable argon atom is rich in the expanded plasma-jet.

The energy levels of the argon atom whose excitation energy is less than 14.7 eV are shown in Fig.7 [19]. The $^3P_2$ and $^3P_0$ levels (11.55 and 11.72 eV, respectively) of the electron configuration $(3p)^5(4s)$ are metastable levels whose optical transition to the $^1S_0$ ground state is forbidden, and the atoms in these levels are known as the metastable argon. On the other hand, the transition from the $^3P_1$ and $^1P_1$ levels to the $^1S_0$ ground state is allowed and these levels have very short life-times [20].

Among the various species produced by arc discharge in the torch, the metastable argon is conserved in the expanded plasma-jet due to its long life-time [21]. Conversely, ions and electrons recombine rapidly because of the drop of the plasma temperature after expansion, and their densities decrease considerably in the expanded plasma-jet [22,23]. The electron temperature of about 4000 K has been obtained by Watson et al. [22] in an expanded plasma-jet, which is similar to the present one. In spite of such a low electron temperature, the expanded plasma-jet radiates intensely the Ar I lines from the $(3p)^5(4p)$ and $(3p)^5(5p)$ states, whose excitation energies are 12.91 to 14.74 eV. It may be expected that these excited states are densely populated by electron impact, as follows [1,7–9],

$$Ar^m + e^- \longrightarrow Ar(3p^5 4p,\ 3p^5 5p) + e^- , \qquad (2)$$

where the necessary energies are 1.2 to 3.1 eV. This is confirmed by the fact that the intensity of Ar I changes in parallel with the metastable argon density as shown in Fig.3. Similarly, ionization may also be possible, because the stepwise ionization from the metastable argon needs only about 4 eV. Therefore, it seems that the highly excited atoms and ions can be produced by the stepwise excitation and ionization from the metastable argon in the expanded plasma-jet.

When admixed hydrogen diffuses into the expanded argon plasma-jet, a fairly large percentage of H_2 will be dissociated into H because of the small dissociation energy of H_2 (4.47 eV). The dissociation takes place thermally and by electron collision;

$$H_2(X\ ^1\Sigma_g^+) \longrightarrow 2H(n=1), \qquad (3)$$

and

$$H_2(X\ ^1\Sigma_g^+) + e^- \longrightarrow 2H(n=1) + e^- , \qquad (4)$$

respectively, where n denotes the principal quantum number. In addition, excitation of the H_2 molecule from the ground state to the first excited state leads to dissociation, because the latter is repulsive.

When both H_2 and H exist in the expanded plasma-jet, the deactivation processes of the metastable argon are as follows;

$$Ar^m + H(n=1) \longrightarrow \begin{cases} Ar(^1S_0) + H(n=2), & (5) \\ Ar(^1S_0) + H(n=3) - 0.37\text{eV}, & (6) \end{cases}$$

$$\mathrm{Ar^m} + \mathrm{H_2}(X\ ^1\Sigma_g^+) \longrightarrow \begin{cases} \mathrm{Ar}(^1S_0) + \mathrm{H_2}(b\ ^3\Sigma_u^+), & (7) \\ \mathrm{Ar}(^1S_0) + \mathrm{H_2}(B\ ^1\Sigma_u^+), & (8) \\ \mathrm{Ar}(^1S_0) + \mathrm{H_2}(c\ ^3\Pi_u) - 0.03\mathrm{eV}, & (9) \\ \mathrm{Ar}(^1S_0) + \mathrm{H_2}(a\ ^3\Sigma_g^+) - 0.07\mathrm{eV}, & (10) \end{cases}$$

where the energy defects are related to $\mathrm{Ar^m}$ ($^3P_0$), so that for $\mathrm{Ar^m}$ ($^3P_2$) 0.17 eV must be added to each value. The energy level diagram of H [19] is shown in Fig.7 and the potential energy curves of H_2 [7] below 12 eV are shown in Fig.8. The collisions (6), (9) and (10) have the energy defects as cited, but these collisions may be nearly resonant processes in consideration of the moderately high temperature in the expanded plasma-jet, because the upper limit of the energy available for the reaction would be the sum of the metastable energy and thermal energy.

The collision (7) leads to the dissociation,

$$\mathrm{H_2}(b\ ^3\Sigma_u^+) \longrightarrow 2\mathrm{H}(n=1), \qquad (11)$$

since the $b\ ^3\Sigma_u^+$ state is repulsive as shown in Fiq.8. $\mathrm{H_2}(B\ ^1\Sigma_u^+)$ produced by the collision (8) emits the Lyman bands [14] in the vacuum ultraviolet region by the following transition,

$$\mathrm{H_2}(B\ ^1\Sigma_u^+) \longrightarrow \mathrm{H_2}(X\ ^1\Sigma_g^+) + h\nu\ (\text{Lyman bands}). \qquad (12)$$

The weak emission around λ 1600 in Fig.6 is identified partly with the Lyman bands. $\mathrm{H_2}(a\ ^3\Sigma_g^+)$ produced by the collision (10) emits the well known continuum extending from λ 1600 to 5000 by the following transition [24],

$$\mathrm{H_2}(a\ ^3\Sigma_g^+) \longrightarrow \mathrm{H_2}(b\ ^3\Sigma_u^+) + h\nu\ (\text{continuum}), \qquad (13)$$

and then the collision (10) also leads to the dissociation of H_2 by the process (11). $H_2(c\ ^3\Pi_u)$ produced by the collision (9) is metastable and dissociates probably by the following process comparable to (3) and (4),

$$H_2(c\ ^3\Pi_u) \longrightarrow H(n=1) + H(n=2), \qquad (14)$$

because of its small dissociation energy (2.29 eV). The inverse process is unusual because of the short life-time of $H(n=2)$. Furthermore, it has been proved that in the expanded plasma-jet the $(3p)^5(4p)$ states of argon transfer efficiently their excitation energy to H by the following collision [23],

$$Ar(3p^5 4p) + H(n=1) \longrightarrow Ar(^1S_0) + H(n\leq 5). \qquad (15)$$

It seems that this process tends to the production of $H(n=4$ and $5)$, that is, the emission of H_β and H_γ as shown in Fig.2.

The population of $H(n=2)$ which emits Lyman α by the following transition,

$$H(n=2) \longrightarrow H(n=1) + h\nu \text{ (Lyman } \alpha), \qquad (16)$$

may be enhanced mainly by the collision (5) and partially by the collisions (9) and (15). In addition to this, the following transition through the Balmer series,

$$H(n\geq 3) \longrightarrow H(n=2) + h\nu \text{ (Balmer series)}, \qquad (17)$$

may contribute to the emission of Lyman α.

It has been known for many years that the Wigner spin conservation

rule is of prime importance for the collisional transfer of electronic energy [16], though the rule is also known to be violated in some cases. According to this rule, no change of total spin occurs in the collision. The rule has been observed to be more impotant than whether or not the transition is optically permitted [18]. Ar($^1S_0$) and Ar^m are singlet and triplet, respectively, and Ar($3p^5 4p$) consists of the singlet and triplet states [19]. All the levels of H are doublet. Therefore, the collision (8) alone violates the Wigner spin conservation rule, among all the energy transfer collisions listed above. This fact results in the negligibly weak intensity of the Lyman bands ($B\ ^1\Sigma_u^+ \longrightarrow X\ ^1\Sigma_g^+$) from the present light source, as shown in Fig.6.

On the contrary, the $B\ ^1\Sigma_u^+$ state can be efficiently excited by electron-impact in the conventional H_2 discharge, and therefore the Lyman bands are intensely emitted over the wide wavelength region in the vacuum ultraviolet [14]. Such a emission is well-known as “the many-lined molecular hydrogen spectrum”.

In conclusion, the selective excitations of H and H_2 by the second-kind collisions with metastable argon lead to the intense and monochromatic emission of Lyman α from the present light source.

(5) Comparison with Microwave-Powered Sources

In the past years, a monochromatic light source of Lyman α has usually been made by microwave-powered discharge in a mixed gas. For instance, Warneck [25] obtained a monochromatic Lyman α source with an 125 W microwave discharge in the He–H_2 mixture, and found the 38% H_2 and He mixture at 0.15 Torr to be best. The total Lyman α intensity was at least 2×10^{15} quanta/s through a LiF window, which was sealed to the end of a Pyrex discharge tube 12.8 mm in outer diameter. Similarly, Okabe [26] obtained an almost pure Lyman α source with 60 W microwave discharge through the 10% H_2 and Ar mixture. The total Lyman α intensity was 3×10^{14} quanta/s through a 78 mm^2 LiF window. His spectrum shows fairly intense emission lines due to impurities, in addition to Lyman α. According to Samson [15], the spectrum in the case of a 25% H_2 and He mixture at 0.2 Torr exhibits a weak continuous emission from λ 1100 to 1300 and an emission of the Lyman bands around λ 1600, in addition to Lyman α.

The spectrum obtained by the present source has a very weak emission of the Lyman bands from λ 1530 to 1700 but no other emission than Lyman α below λ 1530, as shown in Fig.6. The simple structure of this spectrum originates in the selective excitation of H and probably H_2 by the second-kind collisions with the metastable argon. On the contrary, it seems possible in the microwave-powered light source that H

and H_2 are excited not only selectively by the second-kind collision but also not selectively by electron-impact, and moreover impurities are also excited because of a closed discharge tube. As a result, it may be concluded that the present light source of Lyman α using expanded plasma-jet is more monochromatic than conventional.

(6) Conclusion

A highly monochromatic light source of Lyman α has been made by means of the technique of an expanded argon plasma-jet admixed with hydrogen. The monochromatic property and intensity of Lyman α are superior to those obtained by the conventional microwave-powered light source. This light source will be applied successfully to the experimental studies on photon-molecule collisions, such as high-resolution spectroscopy of the secondary emission and photo-electron spectroscopy.

Lyman α occupies 55 % of the solar radiation intensity below λ 1500 [27], and reaches the lower altitude of about 70 km due to the transmission "window" of the Earth's absorption spectrum [28]. Therefore, the present light source will be useful for the laboratory studies on the photochemical and photoionization processes in the upper atmosphere.

References

1) L.E. Brewer and W.K. McGregor: Phys. Fluids **5** (1962) 1485.
2) D.A. Patterson and W.H. Vaughan: J. Opt. Soc. Amer. **53** (1963) 851.
3) P. Warneck: J. Opt. Soc. Amer. **55** (1965) 921.
4) B.J. Spence: *Measurement of Radiant Energy* ed. W.E. Forsythe (McGraw-Hill, New York, 1937) p.198.
5) E.J. Gillham: Research **12** (1959) 404.
6) R.W.Ditchburn: Proc. Roy. Soc. **A229** (1955) 44.
7) L.E. Brewer and W.K. McGregor: *6th International Conference on Ionization Phenomena in Gases* (SERMA, Paris, 1963) Vol.l, p. 263.
8) I. Yamashita and T. Yamanishi: J. Mech. Lab. **21** (1967) 26.
9) I. Yamashita: J. Mech. Lab. **23** (1969) 14.
10) A.C.G. Mitchell and M.W. Zemansky: *Resonance Radiation and Excited Atoms* (Cambridge Univ. Press, London, 1934).
11) I. Yamashita: J. Spectrosc. Soc. Japan **21** (1972) 180.
12) I. Yamashita: J. Phys. Soc. Japan **32** (1972) 1447.
13) I. Yamashita: J. Mech. Eng. Lab. **26** (1972) 41.
14) G. Herzberg and L.L. Howe: Can. J. Phys. **37** (1959) 636.
15) J.A.R. Samson: *Techniques of Vacuum Ultraviolet Spectroscopy* (John Wiley, New York, 1967).
16) H.S.W. Massey: *Electronic and Ionic Impact Phenomena* (Clarendon Press, Oxford, 1971) Vol.3.

17) J.B. Hasted: *Physics of Atomic Collisions*, 2nd ed. (Buttcrworth, London,1972).

18) J.F. Prince, C.B. Collins and W.W. Robertson: J. Chcm. Phys. **40** (1964) 2619.

19) C.E. Moore: *Atomic Energy Levels*, Vol.l, Circular No. 467 (Nat. Bur. Stand., Washington, 1949).

20) W.L. Wiese, M.W. Smith and B.M.Miles: *Atomic Transition Probabilities*, Vol. II , NSRDS-NBS 22 (1969) p. 187.

21) E. Ellis and N.D. Twiddy: J. Phys. **B2** (1969) 1366.

22) M.D. Watson, H.I.S. Ferguson and R.W. Nicholls: Can. J. Phys. **41** (1963) 1405.

23) V.M. Goldhalb, E.V. Ilyina, I.E. Kostygova, G.A. Lukyanov and V.A. Silantyev: Opt. Spectry. **20** (1966) 602.

24) G. Herzberg: *Spectra of Diatomic Molecules* (D. Van Nostrand, New York, 1950).

25) P. Warneck: Appl. Optics **1** (1962) 721.

26) H. Okabe: J. Opt. Soc. Amer. **54** (1964) 478.

27) S.L. Miller and H.C. Urey: Science **130** (1959) 245.

28) A.E.S. Green and P.J. Wyatt: *Atomic and Space Physics* (Addison Wesley, Massachusetts, 1965).

Figure Captions

Fig.1 The light source apparatus of the plasma-jet type. Lyman α is emitted from the expanded argon plasma-jet admixed with H_2, and condensed on the center of the observation chamber through the LiF window and the light guide.

Fig.2 Visible spectra emitted from the expanded plasma-jet as a function of the H_2 flow rate Q_{H2}. The Ar flow rate was 15 l/min and the arc input power 4.0 kW. These spectra were taken with the same sensitivity, and the vertical scale is same for these cases.

(a) Q_{H2} = 0 l/min, (b) Q_{H2} = 0.5 l/min, (c) Q_{H2} = 1.5 l/min

Fig.3 Variations of the fractional absorption for Ar I λ 6965 and line intensities of Ar I λ 6965 and H λ 6563 with the H_2 flow rate Q_{H2}. The Ar flow rate was 15 l/min and the arc input power 4.0 kW.

Fig.4 Variations of the line intensities of Ar I λ 4159, H_α λ 6563 and Lyman α λ 1216 with the H_2 flow rate Q_{H2} for different Ar flow rates Q_{Ar}'s; 10, 15 and 20 l/min. The arc input power was 3.2 kW.

(a) Ar I λ 4159, (b) H_α λ 6563, (c) Lyman α λ 1216.

Fig.5 Variations of the line intensities of H_α λ 6563 and Lyman α λ 1216 with the arc current of the plasma-jet torch. The arc voltage was 20 V, the Ar flow rate 20 l/min and the H_2 flow rate 1.5 l/min.

Fig.6 The spectral characteristics of the light source in the vacuum ultraviolet. This spectrum was taken under the best conditions of the expanded plasma-jet to obtain the intense and monochromatic emission of Lyman α; arc input power 4.0 kW, Ar flow rate 15 l/min and H_2 flow rate 0.5 l/min. The weak emission around λ 1600 is attributed to the Lyman bands of H_2.

Fig.7 The energy level diagrams of Ar and H [19] and the transitions concerned. The metastable states of Ar are denoted by Ar^m.

Fig.8 The potential energy curves of H_2 below 12 eV [17]. The transition $B\ ^1\Sigma_u^+ \longrightarrow X\ ^1\Sigma_g^+$ gives the Lyman bands in the vacuum ultraviolet. The transition $a\ ^3\Sigma_g^+ \longrightarrow b\ ^3\Sigma_u^+$ gives the well-known continuum extending from λ 1600 to 5000.

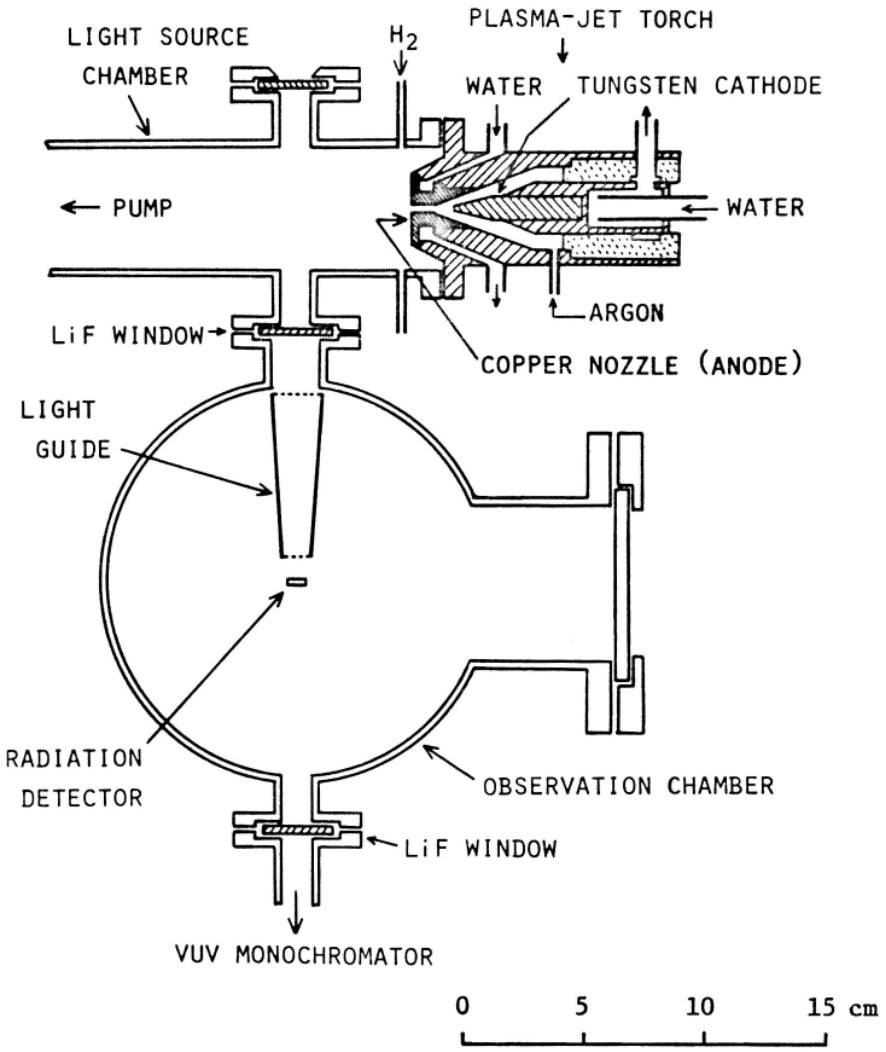

Fig.1 The light source apparatus of the plasma-jet type. Lyman α is emitted from the expanded argon plasma-jet admixed with H_2, and condensed on the center of the observation chamber through the LiF window and the light guide.

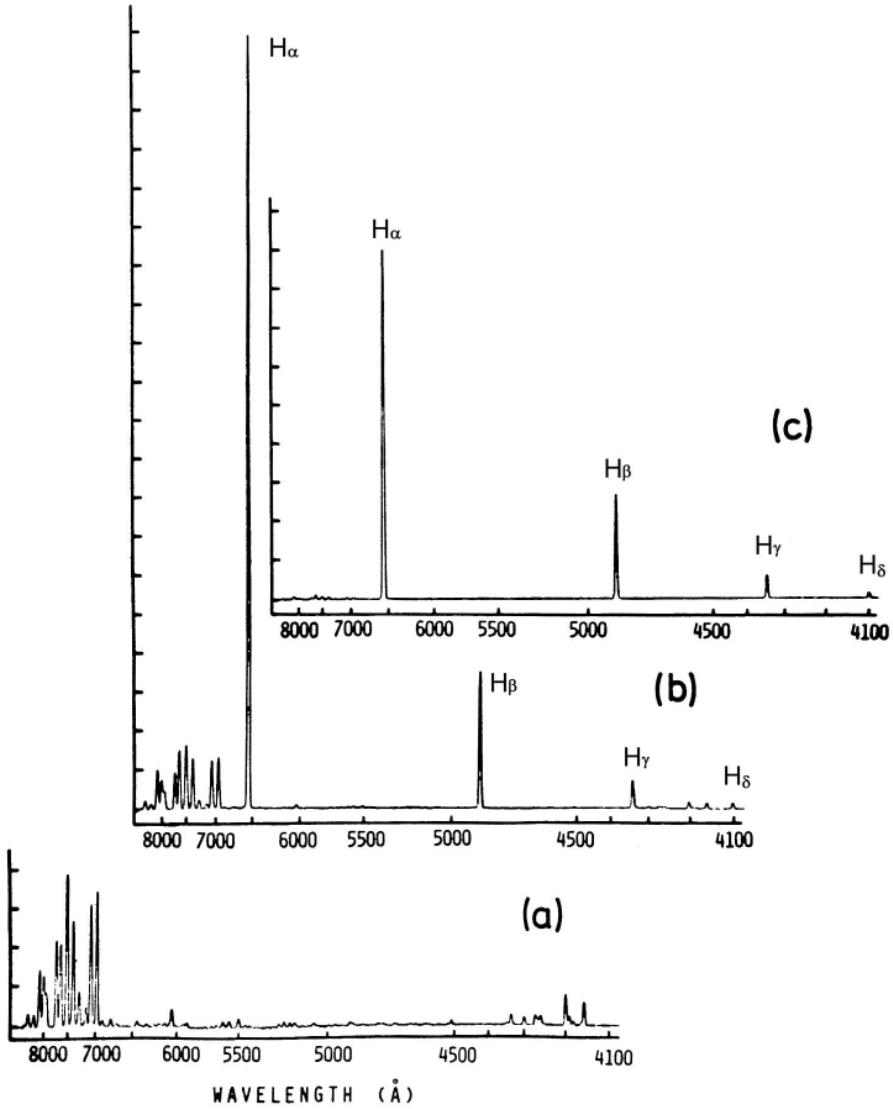

Fig.2 Visible spectra emitted from the expanded plasma-jet as a function of the H_2 flow rate Q_{H2}. The Ar flow rate was 15 l/min and the arc input power 4.0 kW. These spectra were taken with the same sensitivity, and the vertical scale is same for these cases.

(a) Q_{H2} = 0 l/min, (b) Q_{H2} = 0.5 l/min, (c) Q_{H2} = 1.5 l/min

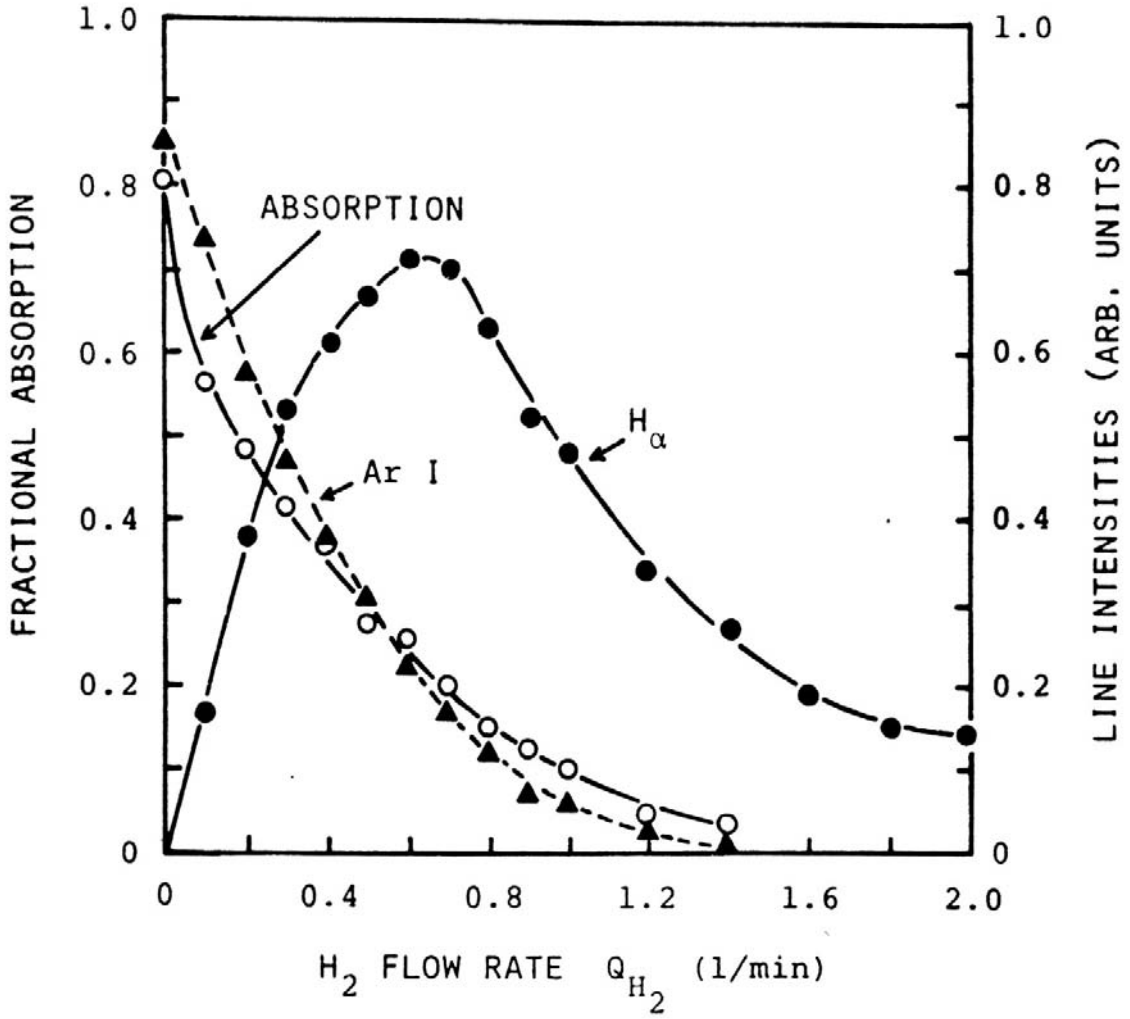

Fig.3 Variations of the fractional absorption for Ar I λ 6965 and line intensities of Ar I λ 6965 and H λ 6563 with the H_2 flow rate Q_{H2}. The Ar flow rate was 15 l/min and the arc input power 4.0 kW.

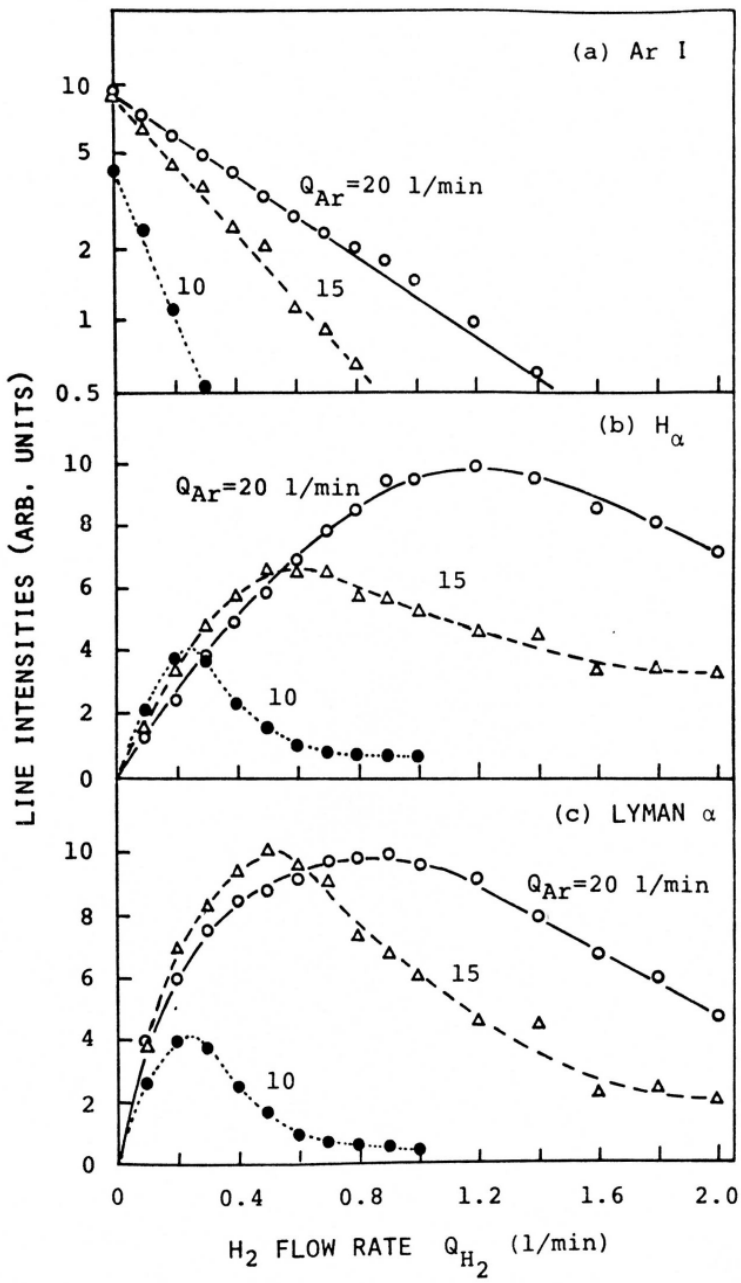

Fig.4 Variations of the line intensities of Ar I λ 4159, H_α λ 6563 and Lyman α λ 1216 with the H_2 flow rate Q_{H2} for different Ar flow rates Q_{Ar}'s; 10, 15 and 20 l/min. The arc input power was 3.2kW. (a) Ar I λ 4159, (b) H_α λ 6563, (c) Lyman α λ 1216.

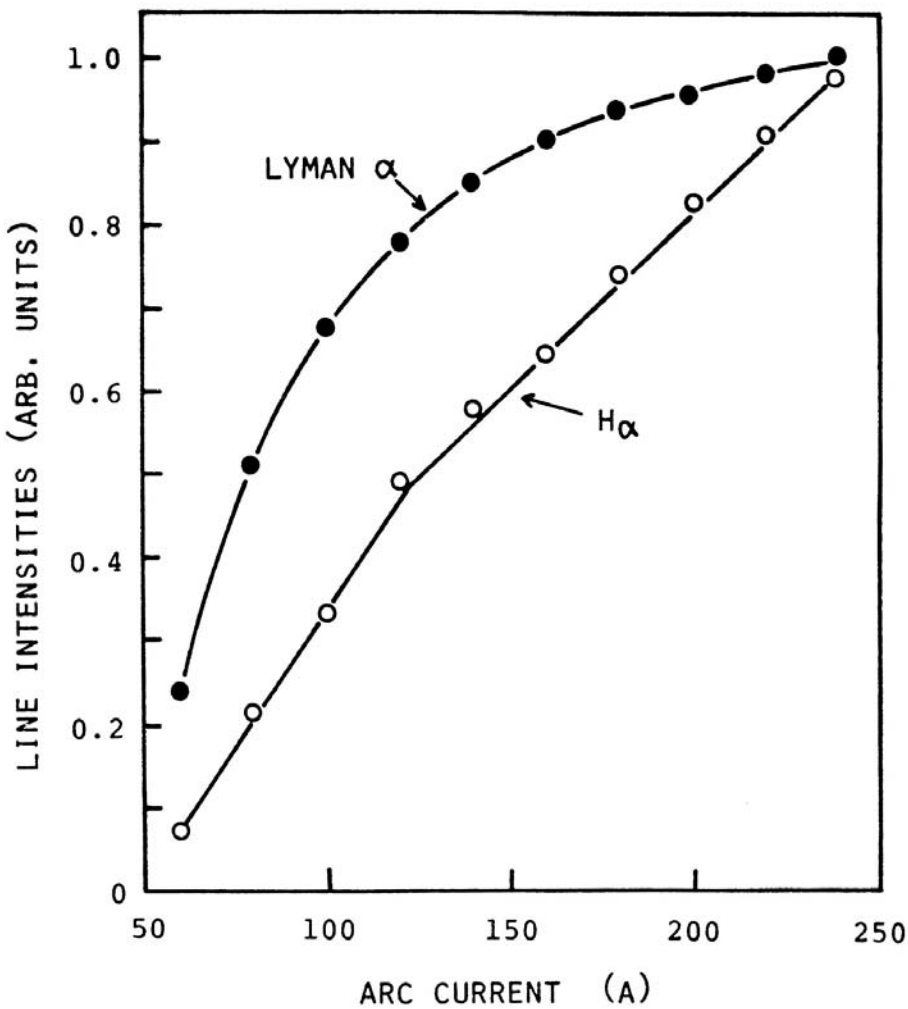

Fig.5 Variations of the line intensities of H_α λ 6563 and Lyman α λ 1216 with the arc current of the plasma-jet torch. The arc voltage was 20 V, the Ar flow rate 20 l/min and the H_2 flow rate 1.5 l/min.

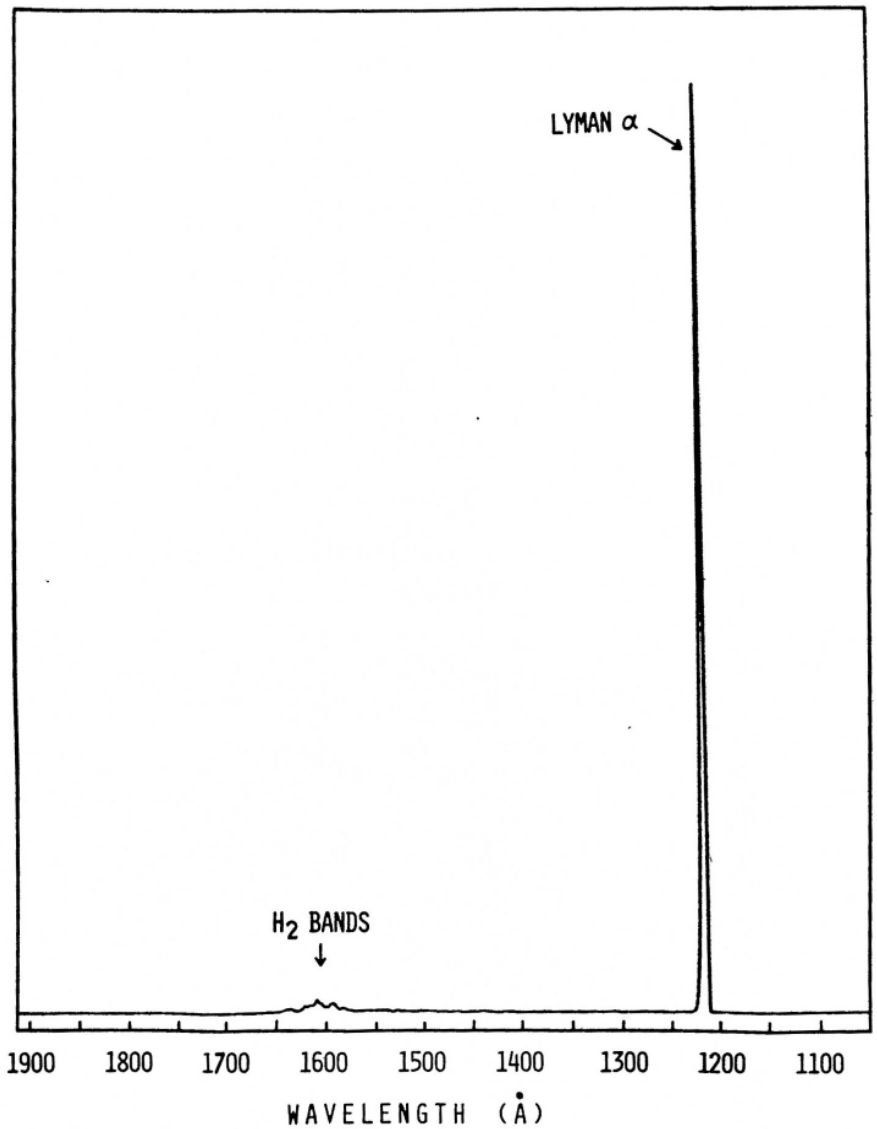

Fig.6 The spectral characteristics of the light source in the vacuum ultraviolet. This spectrum was taken under the best conditions of the expanded plasma-jet to obtain the intense and monochromatic emission of Lyman α; arc input power 4.0 kW, Ar flow rate 15 l/min and H_2 flow rate 0.5 l/min. The weak emission around λ 1600 is attributed to the Lyman bands of H_2.

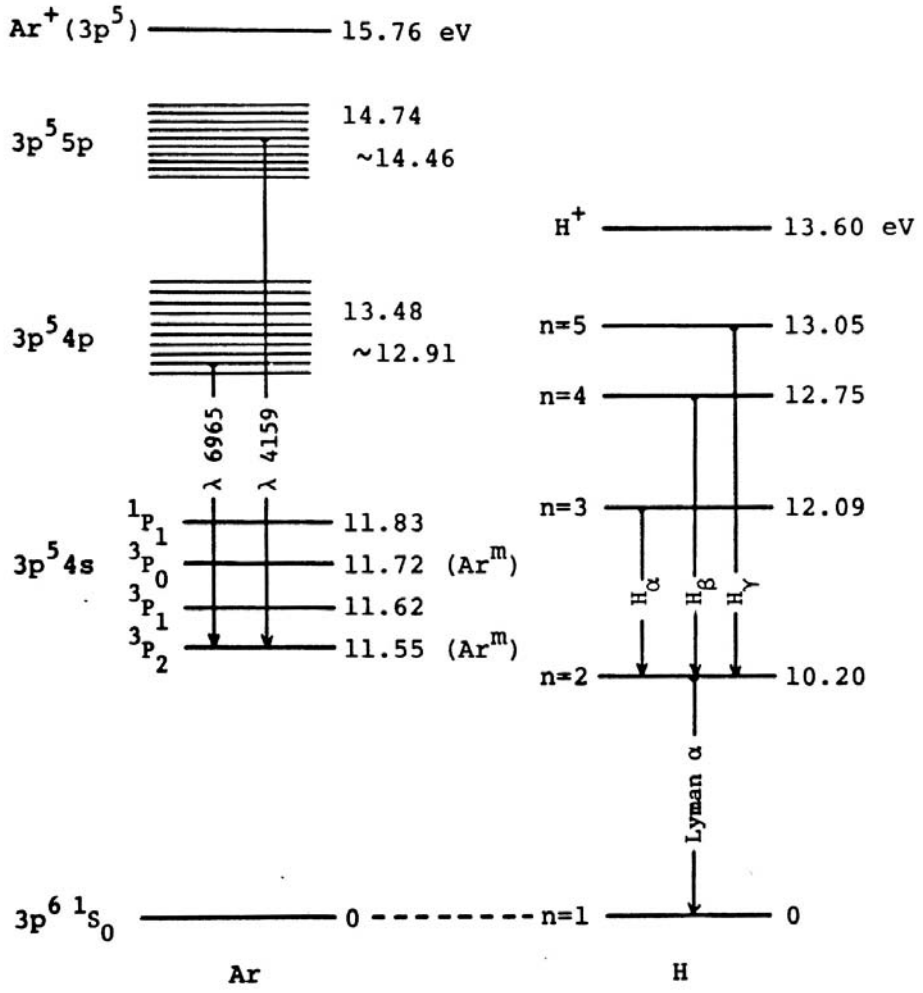

Fig.7 The energy level diagrams of Ar and H [19] and the transitions concerned. The metastable states of Ar are denoted by Ar^m.

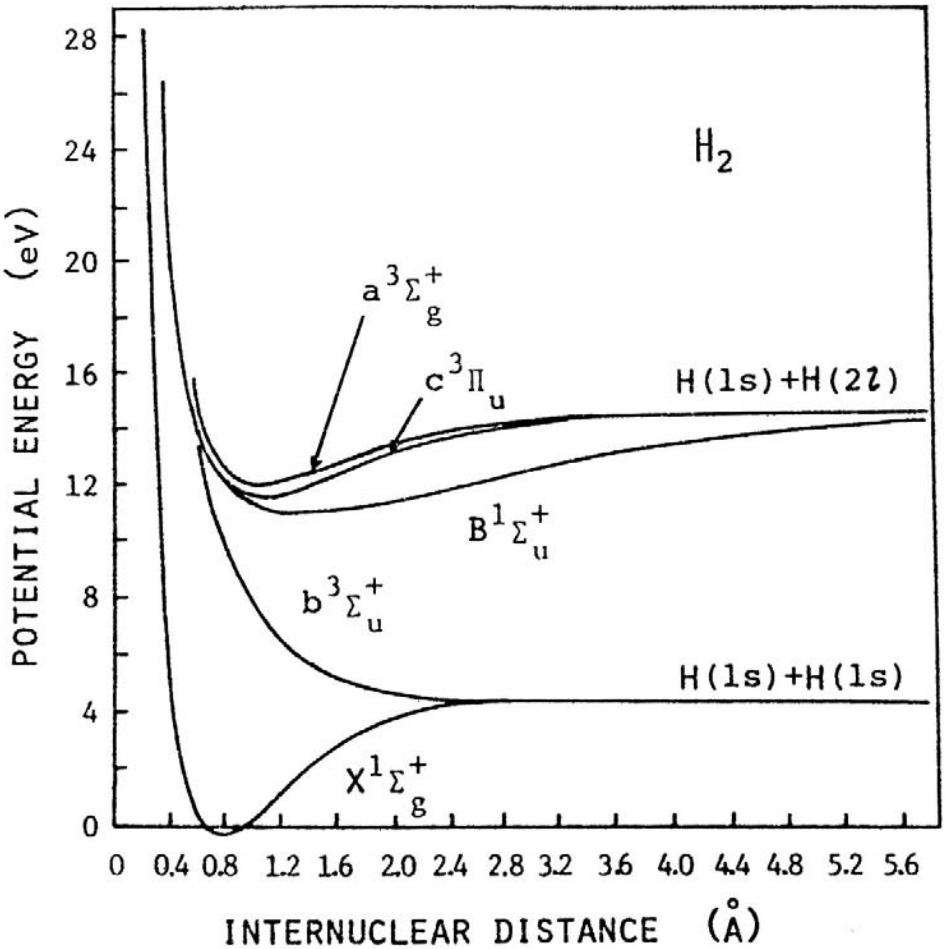

Fig.8 The potential energy curves of H_2 below 12 eV [17]. The transition $B\ ^1\Sigma_u^+ \longrightarrow X\ ^1\Sigma_g^+$ gives the Lyman bands in the vacuum ultraviolet. The transition $a\ ^3\Sigma_g^+ \longrightarrow b\ ^3\Sigma_u^+$ gives the well-known continuum extending from λ 1600 to 5000.

PART II

CROSSED-BEAM EXPERIMENT ON ROTATIONAL POPULATION DISTRIBUTION OF OH ($A\ ^2\Sigma^+$) SPLIT FROM H_2O BY LYMAN ALPHA PHOTON IMPACT

(1) Introduction

Several attempts have so far been made at spectroscopic study on primary rotational population distribution exhibited by OH radical in the $A\ ^2\Sigma^+$ state split from H_2O irradiated by photons in the vacuum ultraviolet region. Some typical distribution curves have been presented by Tanaka et al.[1)], by Carrington[2)], and by Welge et al.[3)], independently. Experiments were all carried out in the target-gas method, as follows.

Flowing H_2O vapor, either pure or diluted with argon, at room temperatures and at reduced pressures is illuminated through a LiF window with light from an exciting light source for use in the vacuum ultraviolet region. The light source is usually a high frequency electrodeless discharge in a flowing gas whose composition, pressure and flow rate are made convenient to a monochromatic vacuum ultraviolet emission.

Generally, all the distribution curves consist of a plateau in the lower range of the rotational quantum number K' and a peak in the

higher range of K'. The relative height of the plateau against the peak varies from each other. Needless to say, these curves were obtained by means of different fluorescence cells and different exciting light sources, under different conditions. As a result, these examples tell how the rotational population distribution considered is sensitive to experimental conditions. That is, in the target-gas method the initial distribution may be disturbed by many ambiguous effects, such as wall-effect, rotational relaxation, electronical quenching and secondary production, as discussed in the following sections.

In the crossed-beam method, these secondary effects may be removed due to the absence of any "wall", the reduced beam density and the rapid convection in the molecular beam. Therefore, it is most important to carry out the same measurement by means of the crossed-beam technique. However, this method gives very weak signals from collision products, because the beam density is considerably low and the effective condensation of light on the molecular beam is difficult in the vacuum ultraviolet. For that purpose, accordingly, it is prerequisite for one to prepare for a monochromatic light source whose intensity is as strong as possible.

Several years ago, the present author was engaged in a study on a characteristics of a supersonic argon plasma jet flow into a vacuum chamber made of a glass cylinder, which was 30 cm in diameter and 1.5 m in length, through a de Laval nozzle. When hydrogen gas was injected into the flow, the supersonic flow extending over almost whole length of

the chamber suddenly shrank into a short flame of 15 cm or so. At the same time, the short flame emitted very strong scarlet radiation composed mainly of the first Balmer line H_α.

The lower state of H concerning the emission of H_α has the principal quantum number n=2. Accordingly, such a scarlet flame must be a very intensive light source of Lyman α λ 1216, since Lyman α is due to the transition from n=2 to n=1. Details of an application of the monochromatic Lyman α light source of the plasma-jet type to a spectroscopic study on the rotational population distribution of $OH(A\ ^2\Sigma^+)$ by the crossed-beam technique will be described in what follows.

(2) Crossed-Beam Apparatus

In the present experiment, a beam of photons from a Lyman α light source and a water molecular beam intersect each other at right angles in a well evacuated collision chamber. Arrangements of the exciting light source, the molecular beam source, and the collision chamber can be seen in Photo.l, Fig.1 and Fig.2. The exciting light beam needs to be not only monochromatic but also as strong as possible. Such an intense light source has been obtained by using an expanded argon plasma-jet admixed with hydrogen. Its details have been described in Part I.

When this light source is used together with a LiF window, its emission spectrum is found to be only Lyman α below λ 1530, as shown in Fig.3. Since any light of longer wavelengths than λ 1350 can not produce OH($A\ ^2\Sigma^+$) from H_2O [2], the present exciting light source enables one to observe the OH radical in the $A\ ^2\Sigma^+$ state split from H_2O irradiated only by Lyman α photons.

Practically, the beam of Lyman α photons is projected on the molecular beam through a LiF window of 1.5 mm in thickness and 12 mm in diameter. Absolute intensity measurements for the Lyman α beam can be made with a thermal detector, which is similar to the Coblentz radiometer [4,5], set in the place of the molecular beam. The intensity measured is 2×10^{15} quanta/cm^{2}s at the distance of 10 cm from the LiF window, as shown in Part I.

By the way, the Lyman α beam is condensed effectively by a "light guide" upon the molecular beam, as shown in Fig.2. The light guide is a truncated regular pyramid in shape. The entrance area is 20×20 mm^2, the exit area 10×10 mm^2, the length 65 mm, and the inner surface is evaporated with aluminium and coated with MgF_2.

Water vapor is led into the collision chamber through a nozzle from a reservoir, and the molecular beam is formed. The nozzle consists of a bundle of fourteen stainless steel pipes. The inner diameter and length of each pipe are 0.6 mm and 5.5 mm, respectively. The cross-sectional area of the nozzle is about 7.0×2.0 mm^2. The beam profile is obtained by measuring the spatial distribution of the OH ultraviolet emission resulting from the collision between the molecular beam and the Lyman α beam, as shown in Fig.4. The half-width of the molecular beam is estimated at 11.2 mm. The peak beam density is estimated at about 0.02 Torr, by comparing the brightness of the crossing with the same brightness in the target-gas method. In the target-gas method, the vapor pressure can be determined by measuring the fractional absorption of Lyman α by H_2O [6].

The collision chamber is made of stainless steel and its inner diameter is 160 mm. The pumping system is composed by a liquid nitrogen trap, a 4 inch diffusion pump and a rotary pump. However, rapid pumping is made mainly by the trap of 2.1 liters in volume. For

effective condensation of water vapor, the trap is double-walled. The inner diameter is 25 mm, the outer diameter 90 mm and the height 370 mm.

The ultraviolet emission of OH($A\ ^2\Sigma^+$) is observed in the direction orthogonal to both the beams. The light flux coming out of the crossing is focused on the slit of 1.0 m Ebert type monochromator (Shimadzu GE-100) by a fused quartz lens and a concave mirror, as shown in Fig.2. The grating has 1200 grooves/mm with a ruled area 52×52 mm^2 and is blazed at 5000 A. The reciprocal linear dispersion is 8.3 Å/mm in the first order. The scanning speed is 5 Å/min. With the slit-width of 50 μm, the resolution is about 0.45 Å, which is defined as the apparent width of a sharp line at half intensity.

Intensity measurements are made with the aid of a photomultiplier (HTV R446) combined with a DC amplifier (Keithley 610C) and a pen-recorder with an integrating time of 2 s. The photomultiplier is used at an applied voltage of 700 V and a dark current 3 pA. The DC amplifier has been found to give a better signal-to-noise ratio than a lockin amplifier (NF LI-572B) in the present experiment. Relative spectral sensitivity of the detection system employed is calibrated against a standard lamp (GE 30A/T24/7).

Transmittance of the LiF window decreases gradually while observations are going on. In order to calibrate the effect resulting from

such a gradual decrease, one has to monitor the integrated intensity of the OH ultraviolet emission with a photomultiplier (HTV R212) in conjunction with a λ 3080 interference filter, as shown in Fig.2. In such a way, one can calibrate the effects of fluctuations in the light source intensity and in the molecular beam density, too. In addition, for checking the stability of the light source, its emission intensities of H_α and Lyman α are monitored by a λ 6560 interference filter and a 50 cm radius Seya-Namioka type monochromator, respectively.

(3) Experimental Results

In order to avoid ambiguous effects of secondary processes inherent in the conventional target-gas method and to see the initial rotational population distribution of OH($A\ ^2\Sigma^+$), the present author has made use of the crossed-beam technique. An example of the pen-recorder traces for the OH, $A\ ^2\Sigma^+ \longrightarrow X\ ^2\Pi$ band-system is presented in Fig.5. In this spectrum, the six main branches of the (0,0) band designated by P_1, P_2, Q_1, Q_2, R_1 and R_2 are dominant, and the distinct head at λ 3064 corresponds to the head of the R_1 branch. In addition, the (1,1) band can be recognized. It can also be recognized that the rotational line intensity of the (0,0) band drops abruptly at K'=23 for each main branch.

The rotational populations can be derived from the line intensities by use of the transition probabilities tabulated by Learner [7]. The rotational population distributions obtained for the vibrational states of

v' = 0 and 1 are shown in Figs.6 and 7, respectively. The rotational populations; $N_0(K')$ for v' = 0 and $N_1(K')$ for v' = 1 are normalized so that the averaged population of K' = 21 for v' = 0; $\langle N_0(21)\rangle$ is unity. The rotational lines available for plotting these figures are selected by taking the resolution attained into consideration, in comparison with the table given by Dieke et al.[8] and the atlas presented by Bass et al.[9]. They are as free as possible from overlapping with other lines.

When compared with each other, a remarkable difference can be seen between Figs.6 and 7. There are two reasons why such a difference exists. One is the definite energy possessed by the Lyman α photon and the other the predissociation inherent in OH ($A\ ^2\Sigma^+$). The excess energy available for excitation of vibration and rotation of OH ($A\ ^2\Sigma^+$) resulting from the following collision,

$$H_2O(\widetilde{X}\ ^1A_1) + h\nu\ (\text{Lyman } \alpha) \longrightarrow OH\ (A\ ^2\Sigma^+) + H\ (^2S), \qquad (1)$$

can be estimated at 1.06 eV by subtracting the dissociation energy of H_2O and the electronic excitation energy of OH from the energy of Lyman α, as shown in Fig.8. It gives the highest rotational levels possible; K'=22 for v'=0 and K'=18 for v'=1, respectively. The abrupt drop between K'=22 and 23 as shown in Fig.6 is in good agreement with the above estimation.

Similarly, a peak may be expected to appear at K'=18 in the distribution curve for v'=l, too, as indicated by the dotted line curve in Fig.7. Actually, however, the population decreases promptly with

increasing K' above 15. Such a discrepancy may be due to the predissociation of OH($A\ ^2\Sigma^+$), which has so far been studied by many authors, since it was discovered by Gaydon et al. in 1951 [10]. The most detailed experimental study on it has recently been carried out by Sutherland et al.[11]. They have measured the life-times of the individual rotational levels of OH($A\ ^2\Sigma^+$), making use of an interrupted rf discharge through water vapor. According to them, the predissociation occurs at K'=23 for v'=0, while it takes place at K'=14 for v'=1. Further discussions on the predissociation are given in Appendix A.

(4) Theoretical Interpretation

The rotational population distributions of OH($A\ ^2\Sigma^+$) in the vibrational states of v'=0 and 1 have been obtained by the crossed-beam technique, as presented in Figs.6 and 7. The distribution curve in the case of v'=1 is considerably affected with the predissociation effect. However, the predissociation is inherent in OH($A\ ^2\Sigma^+$) radical itself. Accordingly, Figs.6 and 7 may be considered to show the initial rotational population distributions of OH($A\ ^2\Sigma^+$) split from H_2O by the Lyman α photon impact.

So far, many experimental and theoretical works have been devoted to the dissociation processes of electronically excited H_2O. Those results have recently been summarized by Tsurubuchi [12]. He has constructed well established correlation diagrams concerning the

dissociation of the singlet and triplet excited states of H_2O, on the basis of experimental evidences, theoretical calculations and symmetry properties of atomic and molecular orbitals. In addition, he has discussed the extremely non-thermal rotation exhibited by OH($A\ ^2\Sigma^+$) split from H_2O bombarded by electron, photon and metastable atom.

In the case of electron impact[13], for instance, the electron exchange collision can take place. Accordingly, the H_2O molecule in the ground state $\widetilde{X}\ ^1A_1$ can be excited not only to singlet states but also to triplet states. In other terms, the rotational behavior of OH($A\ ^2\Sigma^+$) split by electron-impact from H_2O may depend in a complicated manner upon potential surfaces for both singlet and triplet excited states of H_2O.

On the contrary, in the case of photon-impact, the H_2O molecule originally in the singlet ground state can be brought up only to some of the upper singlet states, because of the selection rule of ΔS=0 and the requirement for the excited and ground states symmetries[14].

According to the correlation diagrams drawn by Tsurubuchi[12] (see Appendix B), Lyman α (10.20 eV) is able to excite H_2O to the following singlet states; $\widetilde{B}\ ^1A_1$, $\widetilde{C}\ ^1B_1$, and $\widetilde{D}\ ^1A_1$, because their vertical energies are 9.7, 10.00 and 10.17 eV, respectively. The $\widetilde{B}\ ^1A_1$ state correlates to the dissociation into OH($A\ ^2\Sigma^+$) + H(^2S) in the symmetry of C_s and correlates to O(^1D) + H_2($X\ ^1\Sigma_g^+$) in the symmetry of C_{2v}. The $\widetilde{C}\ ^1B_1$ state correlates to OH($^2\Delta$) +H(^2S) and O(^3P) +H_2($b\ ^3\Sigma_u^+$) in the symmetries of C_s and C_{2v}, respectively. The $\widetilde{D}\ ^1A_1$ state correlates to OH($^2\Delta$) + H(^2S) and

$O(^1S) + H_2(X\ ^1\Sigma_g^+)$ in the symmetries of C_s and C_{2v}, respectively. As a result, only the $\widetilde{B}\ ^1A_1$ state is important for the present purpose.

Referring to the potential energy surfaces of the excited states of H_2O including $\widetilde{B}\ ^1A_1$, theoretical studies have been carried out by Niira in the AO method[15], by Horsley et al. in the ab initio LCAO-MO-SCF method[16], and Claydon et al. in the INDO method[17]. Unfortunately, however, those studies could not supply any sufficient informations about the mechanism of the abnormal rotation of $OH(A\ ^2\Sigma^+)$, because of their lower order approximations. Recently, Flouquet and Horsley have calculated the potential energy surface of the $\widetilde{B}\ ^1A_1$ state by the improved method including configuration interaction[18]. According to them, there is a conical potential valley in the potential surface, whose apex lies at the distance of 1.5 Å apart from the O atom in the linear conformation. It is consistent with the molecular orbital and symmetry considerations proposed by Gangi et al.[19]. More detailed discussions on the potential energy surface are carried out in Appendix B.

Just after excitation by photon-impact, the two H atoms have the same positions with respect to the O atom as in the ground state, according to the Franck-Condon principle, where the internuclear distance between the O and H atoms is 1.0 Å and the bond angle 105°. Then, one of the H atoms will move toward the apex of the conical potential valley. In other terms, the excited H_2O will open out its bond angle, and at the same time the distance between the O atom and the splitting H atom will increase. In that case, each H atom will obtain a

large angular momentum of the same magnitude but in the opposite direction, because of the steep and deep valley. At the present stage, however, any theoretical prediction can not be given of the trajectory for the splitting H atom to take after this.

On the other hand, the experimental result in Fig.6 tells that only the rotational levels around $K'=21$ are preferentially populated. Therefore, according to the law of angular momentum conservation, one of the H atoms must fly off with a large angular momentum with respect to the O atom, and the H atom can not split in any radial direction. In order to come apart from the O atom, the H atom has to climb up the slope of the valley, and loses its linear momentum considerably. The product of the final linear momentum with the vertical distance from the O atom to the tangent of the trajectory along which the splitting H atom becomes free must be equal to the angular momentum of the OH($A\ ^2\Sigma^+$) radical.

(5) Comparison with Target-Gas Experiments

As mentioned in the section (1), the previous results derived by others from the conventional target-gas experiments are not in agreement with each other, especially with respect to relative heights of the plateau and the peak. For the purpose of looking into the reason why so, the present author has applied the present exciting light source of the plasma-jet type to the target-gas experiments.

In order to see whether the rotational population distribution considered suffers from the wall effect or not, he has compared two fluorescence cells different in size. One is 160 mm, and the other 18 mm in diameter. The H_2O vapor pressure is commonly 0.080 Torr. The results obtained coincide with each other, as shown in Fig.9, where $N_0(K')$ is normalized so that $\langle N_0(22)\rangle = 1$. On the other hand, in order to see the pressure effect upon the rotational population distribution considered, he has repeated the same experiment at the vapor pressures of 0.016 and 0.080 Torr in the fluorescence cell of 160 mm in diameter. In that case, the results do not coincide, as shown in Fig.10. The plateau, which is the flat part in the range for $K' \leq 8$, is lower by about 35% in the case of the lower pressure than the other.

Fig.9 tells that there is not any wall effect as fas as the cell is larger than 18 mm in diameter, probably because of the short lifetime and large quenching frequency of $OH(A\,^2\Sigma^+)$ [11]. Encounter of this radical with H_2O in the cell would lead to electronical quenching, as follows,

$$OH\ (A\,^2\Sigma^+) + H_2O \longrightarrow OH\ (X\,^2\Pi) + H_2O. \qquad (2)$$

As for the quenching probabilities, Sutherland et al. have recently shown that they are almost independent of K' [11].

According to Fig.10, the relative population $N_0(K')$ in the lower K' range grows up with increase in the water vapor pressure within the cell.

Experimental evidences quite similar to this have previously been given by Schüler et al. [20–22]. The initial rotational populations of diatomic hydrides such as CuH, AlH and BiH are all relaxed by collisions with inert atoms He and Ar to the Boltzmann distribution corresponding to the inert gas temperature. For instance, the initial rotational temperature of 1800 K exhibited by AlH at the lowest pressure of matrix gas is relaxed gradually with increasing pressures, and finally brought to the Boltzmann distribution corresponding to 800 K. In the present target-gas experiment, abnormally rotating OH($A\,^2\Sigma^+$) is surrounded by H_2O vapor at the room temperature. Such a collisional relaxation may be expected to occur in addition to the electronical quenching mentioned above.

The crossed-beam experimental result is plotted again in the same semi-logarithmic scale as the target-gas result at the lowest pressure 0.016 Torr in Fig.11, for comparison. The number density within the molecular beam in the crossed-beam experiment is estimated at about 0.02 Torr. Notwithstanding that the number densities are nearly the same, there is a disagreement between the two curves. It may be due to the following reason. In the crossed-beam experiment, all kinds of species produced at the intersection of the molecular beam with the beam of photons run off swiftly along the molecular beam, and they never come back to the intersection where light signals to be observed are coming from. On the contrary, in the target-gas experiment, their motions are

quite at random, and, accordingly, long lived fragment species such as OH($X\ ^2\Pi$), H(^2S) and O(^1D), which are born in the target gas along the exciting light path, can diffuse into the space where light signals to be studied are coming from.

For instance, H(^2S) and OH($A\ ^2\Sigma^+$) are produced in the primary collision process (1), where the latter makes a transition with radiation to OH($X\ ^2\Pi$), or it may be quenched without radiation by (2). In addition, OH($X\ ^2\Pi$), H(^2S) and O(^1D) may be produced in the following ways [23,24],

$$H_2O\ (\widetilde{X}\ ^1A_1) + h\nu\ (\leq \lambda\ 1470) \longrightarrow H_2\ (X\ ^1\Sigma_g^+) + O(^1D), \qquad (3a)$$

and

$$H_2O\ (\widetilde{X}\ ^1A_1) + h\nu\ (\leq \lambda\ 1860) \longrightarrow OH(X\ ^2\Pi) + H(^2S), \qquad (3b)$$

where such a photon is contained in the light from the present light source, as seen in Fig.3. Then the following collisions,

$$O(^1D) + H(^2S) + H_2O \longrightarrow OH\ (A\ ^2\Sigma^+) + H_2O, \qquad (4)$$

and

$$OH(X\ ^2\Pi) + h\nu\ (\text{ultraviolet}) \longrightarrow OH\ (A\ ^2\Sigma^+), \qquad (5)$$

may be expected to take place along the path of the exciting light beam within the cell.

According to the statistical model including angular momentum conservation [25,26], the rotational population distribution of OH($A\ ^2\Sigma^+$) radical produced in the three-body collision (4) is expected to be close to the thermal distribution, because the excess energy possessed by the five-atomic intermediate should be partitioned among so many degrees of

freedom of OH and H_2O. In addition, the long-lived radical OH($X\ ^2\Pi$) produced in any way is expected to have the thermal rotational distribution corresponding to the target-gas temperature. The ultraviolet radiation from the present light source is composed mainly of a weak continuum, as shown in Fig.3. Accordingly, the OH($A\ ^2\Sigma^+$) radical produced in (5) can not show any abnormal rotation.

As a result, it may be concluded that the secondary production of OH($A\ ^2\Sigma^+$) in both the processes (4) and (5) contributes to an enhancement of the plateau against the peak, as seen in Fig.11.

(6) Conclusion

Secondary production of OH($A\ ^2\Sigma^+$) due to the long-lived radicals such as OH($X\ ^2\Pi$), H(^2S) and O(^1D) may be able to disturb the primary distribution aimed at, especially in the target-gas method. If the water vapor pressure in the fluorescence cell were reduced by an order of one or two than the lowest pressure attained in the present experiment, such a disturbance would be suppressed more completely. However, light signals available would become too weak to allow any measurement with a simple detection system. On the other hand, in the crossed-beam method, the long-lived radicals will soon be carried away by the convection of the molecular beam. As a result, the curves presented in Figs. 6 and 7 may be as close as possible to the initial rotational

population distributions of OH($A\ ^2\Sigma^+$; v'=0) and OH($A\ ^2\Sigma^+$; v'=l) produced by the primary photon-molecule collision (1).

References

1) I. Tanaka, T. Carrington and H.P. Broida: J. chem. Phys. **35** (1961) 750.
2) T. Carrington: J. chem. Phys. **41** (1964) 2012.
3) K.H. Welge, S.V. Filseth and J. Davenport: J. chem. Phys. **53** (1970) 502.
4) B.J. Spence: *Measurement of Radiant Energy* ed. W.E. Forsythe (McGraw-Hill, New York, 1937) p.198.
5) E.J. Gillham: Research **12** (1959) 404.
6) W.R.S. Garton, M.S.W. Webb and P.C. Wildy: J. Sci. Instr. **34** (1957) 496.
7) R.C.M. Learner: Proc. Roy. Soc. **A269** (1962) 311.
8) G.H. Dieke and H.M. Crosswhite: J. Quant. Spectrosc. Radiat. Transfer **2** (1962) 97.
9) A.M. Bass and H.P. Broida: Nat. Bur. Stand. Circular **541** (1953).
10) A.G. Gaydon and H.G. Wolfhald: Proc. Roy. Soc. **A208** (1951) 63.
11) R.A. Sutherland and R.A. Anderson: J. chem. Phys. **58** (1973) 1226.
12) S. Tsurubuchi: J. Phys. Soc. Japan (to be published).
13) T. Horie, T. Nagura and M. Otsuka: J. Phys. Soc. Japan **11** (1956) 1157; Phys. Rev. **104** (1956) 547.
14) G. Herzberg: *Electronic Spectra and Electronic Structure of Polyatomic Molecules* (Van Nostrand, New York, 1966) Chap.2.

15) K. Niira: J. Phys. Soc. Japan **7** (1952) 193.

16) J.A. Horsley and W.H. Fink: J. chem. Phys. **50** (1969) 750.

17) C.R. Claydon, G.A. Segal and H.S. Taylor: J. chem. Phys. **54** (1971) 3799.

18) F. Flouquet and J.A. Horsley: J. chem. Phys. **60** (1974) 3767.

19) R.A. Gangi and R.F.W. Bader: J. chem. Phys. **55** (1971) 5369.

20) H. Schüler, H. Gollnow and H. Haber: Z. Phys. **111** (1939) 484,508.

21) H. Schüler and H. Gollnow: Z. Phys. **108** (1938) 714.

22) H. Schüler and H. Haber: Z. Phys. **112** (1939) 614.

23) M. Cottin, J. Masanet and C. Vermeil: J. Chim. Phys. **63** (1966) 959.

24) K.H. Welge and F. Stuhl: J. chem. Phys. **46** (1967) 2440.

25) T. Horie and T. Kasuga: J. chem. Phys. **40** (1964) 1683.

26) M. Kimura, S. Watanabe and T. Horie: J. Phys. Soc. Japan **32** (1972) 1348.

Figure Captions

Photo.1 Overall view of the crossed-beam apparatus for the Lyman α photon impact on H_2O.

Fig.1 Schematical diagram of the crossed-beam apparatus (vertical sections). The Lyman α light beam is condensed by the light guide upon the H_2O molecular beam, which is formed by means of a multi-channel nozzle. The rapid pumping of the collision chamber is made mainly by the double-walled liquid-N_2 cold trap.

Fig.2 Schematical diagram of the crossed-beam apparatus (horizontal section). The light source is of the plasma-jet type, and its spectrum is taken with the vacuum ultraviolet monochromator. The OH ultraviolet emission resulting from the collision between the molecular beam and Lyman α beam is observed in the direction orthogonal to both the beams with the 1.0 m Ebert type monochromator.

Fig.3 The spectral characteristics of the light source in the vacuum and near ultraviolet regions.

Fig.4 The H_2O molecular beam profile obtained by measuring the spatial distribution of the OH ultraviolet emission from the intersection between the molecular beam and Lyman α beam. The half-width and the peak density are estimated at 11.2 mm and 0.02 Torr, respectively.

Fig. 5 A pen-recorder trace of the $A\ ^2\Sigma^+$A $\longrightarrow$ $X\ ^2\Pi$ band-system of OH resulting from the Lyman α photon impact on H_2O in the crossed-beam experiment. The (0,0) band is dominant, and the weak (1,1) band is also recognized. Each band is consist of the six main branches designated by P_1, P_2, Q_1, Q_2, R_1 and R_2, whose band-heads are indicated by the hatched-lines.

Fig.6 The rotational population distribution of OH($A\ ^2\Sigma^+$) for the vibrational state of $v' = 0$ obtained by the crossed-beam method. The population with the rotational quantum number K'; $N_0(K')$ is normalized so that the average population at $K' = 21$; $\langle N_0(21)\rangle$ is unity. The abrupt drop between $K' = 22$ and 23 corresponds to the energetical limit (see Fig.8).

Fig. 7 The rotational population distribution of OH($A\ ^2\Sigma^+$) for the vibrational state of $v' = 1$ obtained by the crossed-beam method. The rotational population for $v' = 1$; $N_1(K')$ is normalized in the same way as in Fig.6, that is, $\langle N_0(21)\rangle = 1$.

Fig.8 The energy level diagram related to the Lyman α photon-impact excitation of H_2O leading to OH($A\ ^2\Sigma^+$).

Fig.9 Comparison between the rotational distributions of OH($A\ ^2\Sigma^+$) for $v' = 0$ at the H_2O vapor pressure of 0.080 Torr in the fluorescence cells of the diameters of 160 and 18 mm obtained by the target-gas method. The population $N_0(K')$ is normalized so that $\langle N_0(21)\rangle = 1$.

(a) diameter 160 mm, (b) diameter 18 mm.

Fig.10 Comparison between the rotational distributions of OH($A\ ^2\Sigma^+$) for $v' = 0$ at the H_2O vapor pressures of 0.016 and 0.080 Torr in the fluorescence cell of 180 mm in diameter obtained by the target-gas method. The population $N_0(K')$ is normalized so that $\langle N_0(21)\rangle = 1$.

Fig.11 Comparison of the rotational distribution of OH($A\ ^2\Sigma^+$) for $v' = 0$ obtained by the target-gas method at the H_2O vapor pressure of 0.016 Torr with that by the crossed-beam method. The former is taken from Fig.10, and the latter is the same as Fig.6 except in the semi-logarithmic scale.

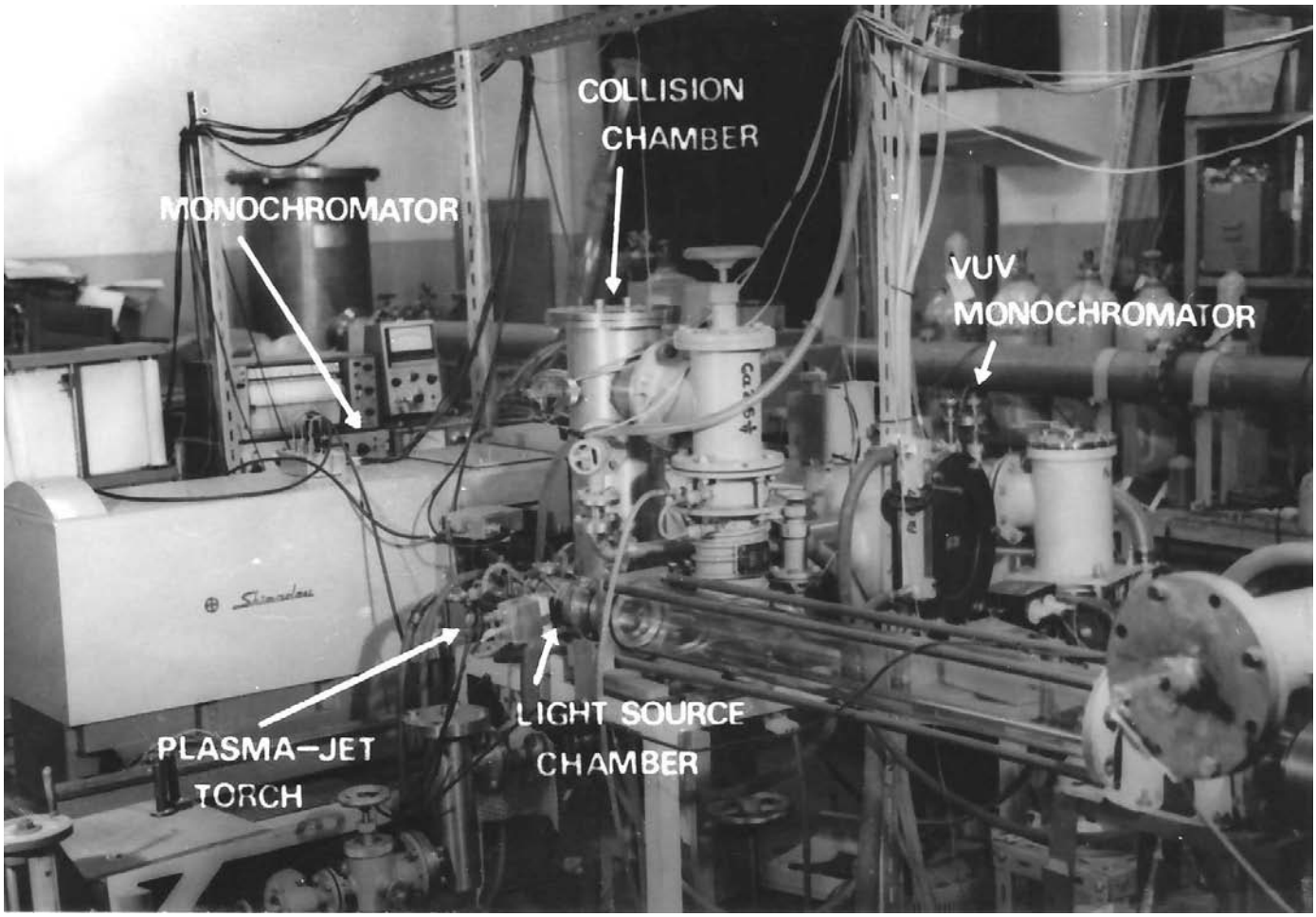

Photo.1 Overall view of the crossed-beam apparatus for the Lyman α photon impact on H_2O.

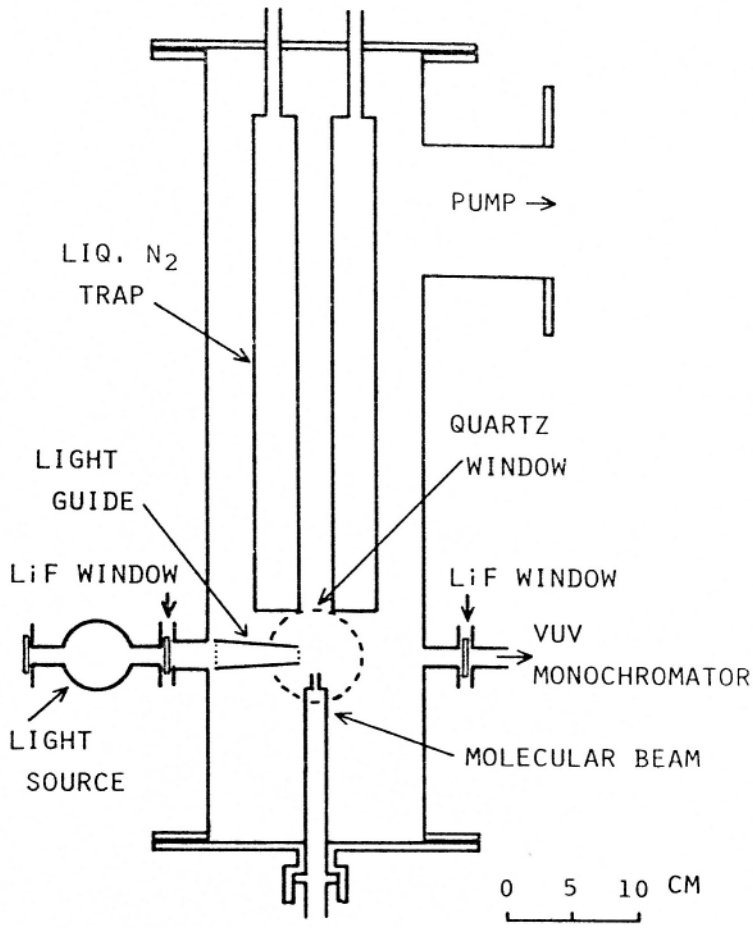

Fig.1 Schematical diagram of the crossed-beam apparatus (vertical sections). The Lyman α light beam is condensed by the light guide upon the H_2O molecular beam, which is formed by means of a multi-channel nozzle. The rapid pumping of the collision chamber is made mainly by the double-walled liquid-N_2 cold trap.

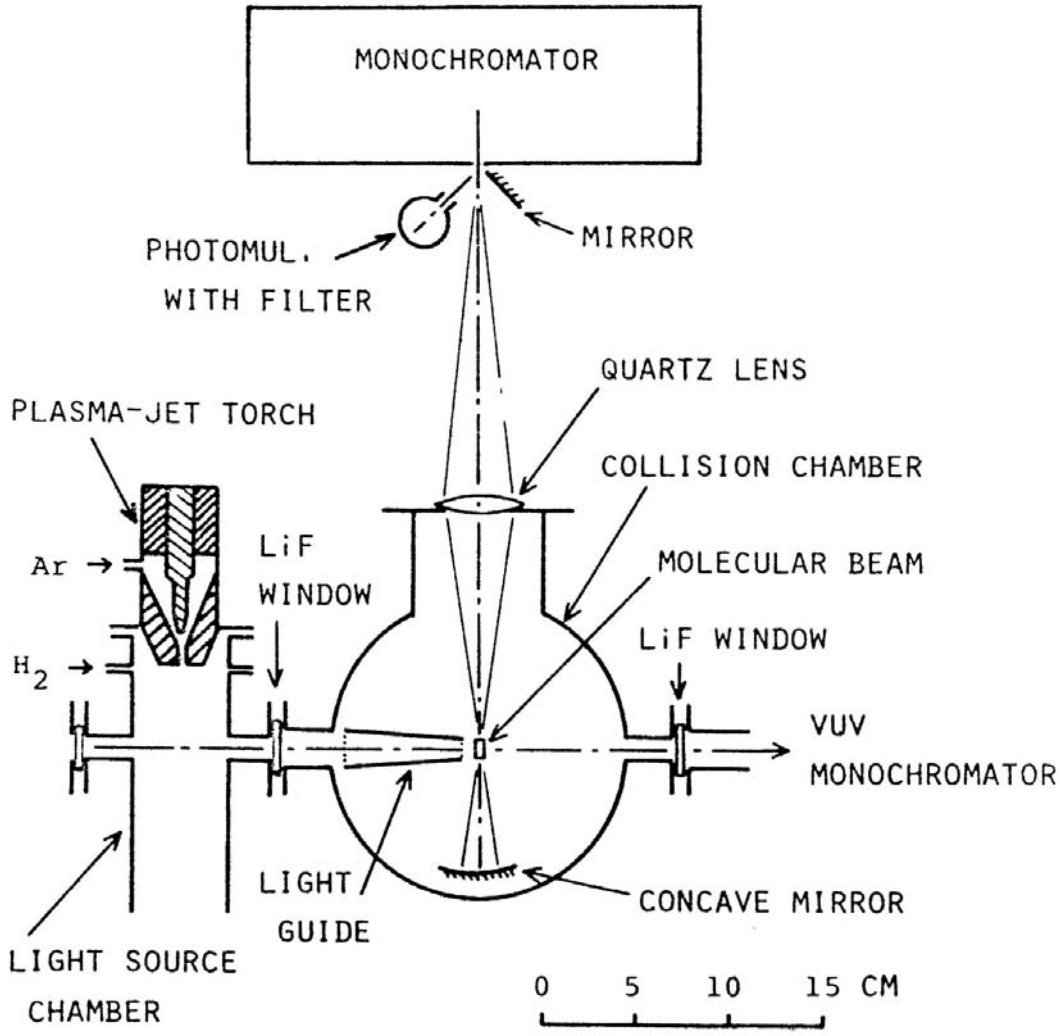

Fig.2 Schematical diagram of the crossed-beam apparatus (horizontal section). The light source is of the plasma-jet type, and its spectrum is taken with the vacuum ultraviolet monochromator. The OH ultraviolet emission resulting from the collision between the molecular beam and Lyman α beam is observed in the direction orthogonal to both the beams with the 1.0 m Ebert type monochromator.

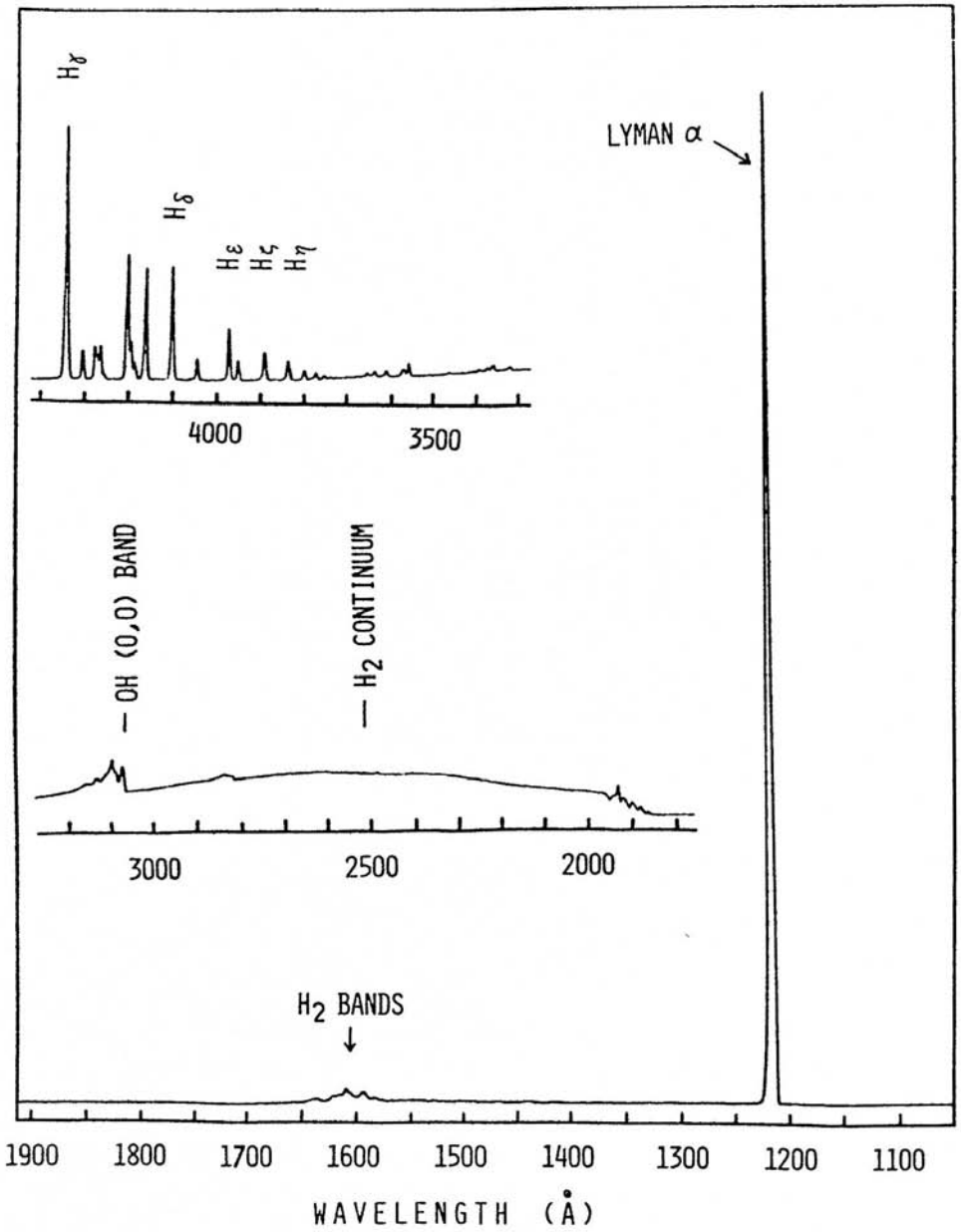

Fig.3 The spectral characteristics of the light source in the vacuum and near ultraviolet regions.

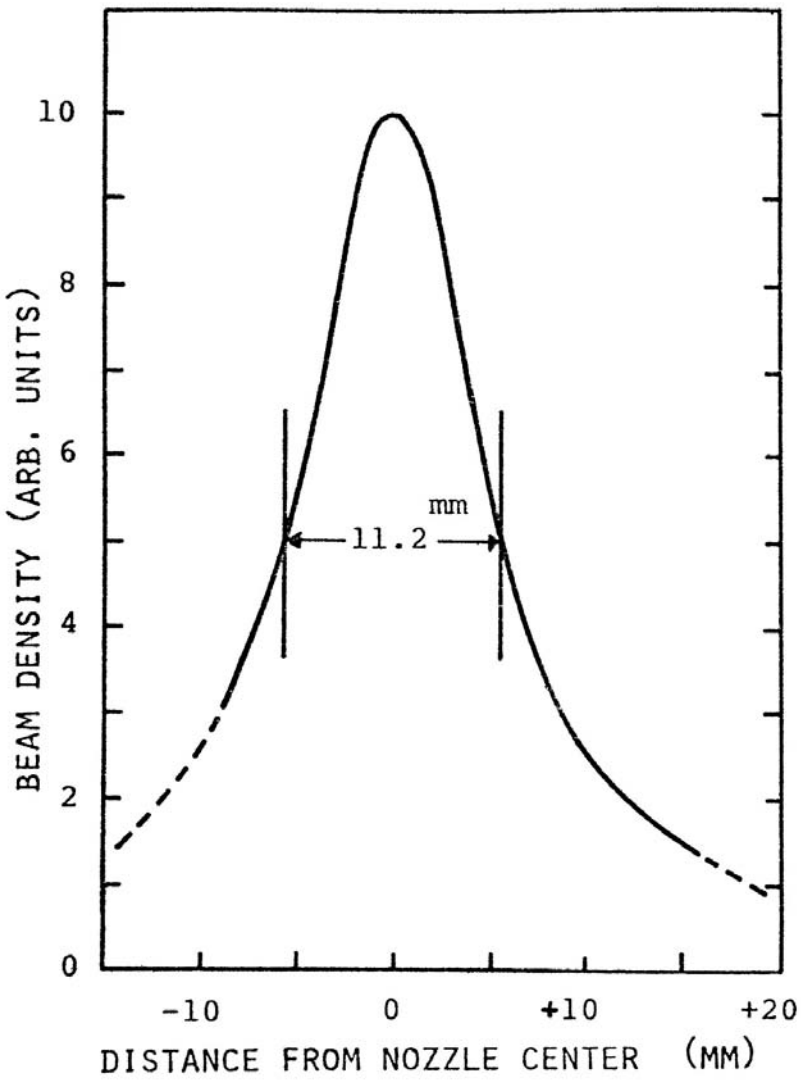

Fig.4 The H_2O molecular beam profile obtained by measuring the spatial distribution of the OH ultraviolet emission from the intersection between the molecular beam and Lyman α beam. The half-width and the peak density are estimated at 11.2 mm and 0.02 Torr, respectively.

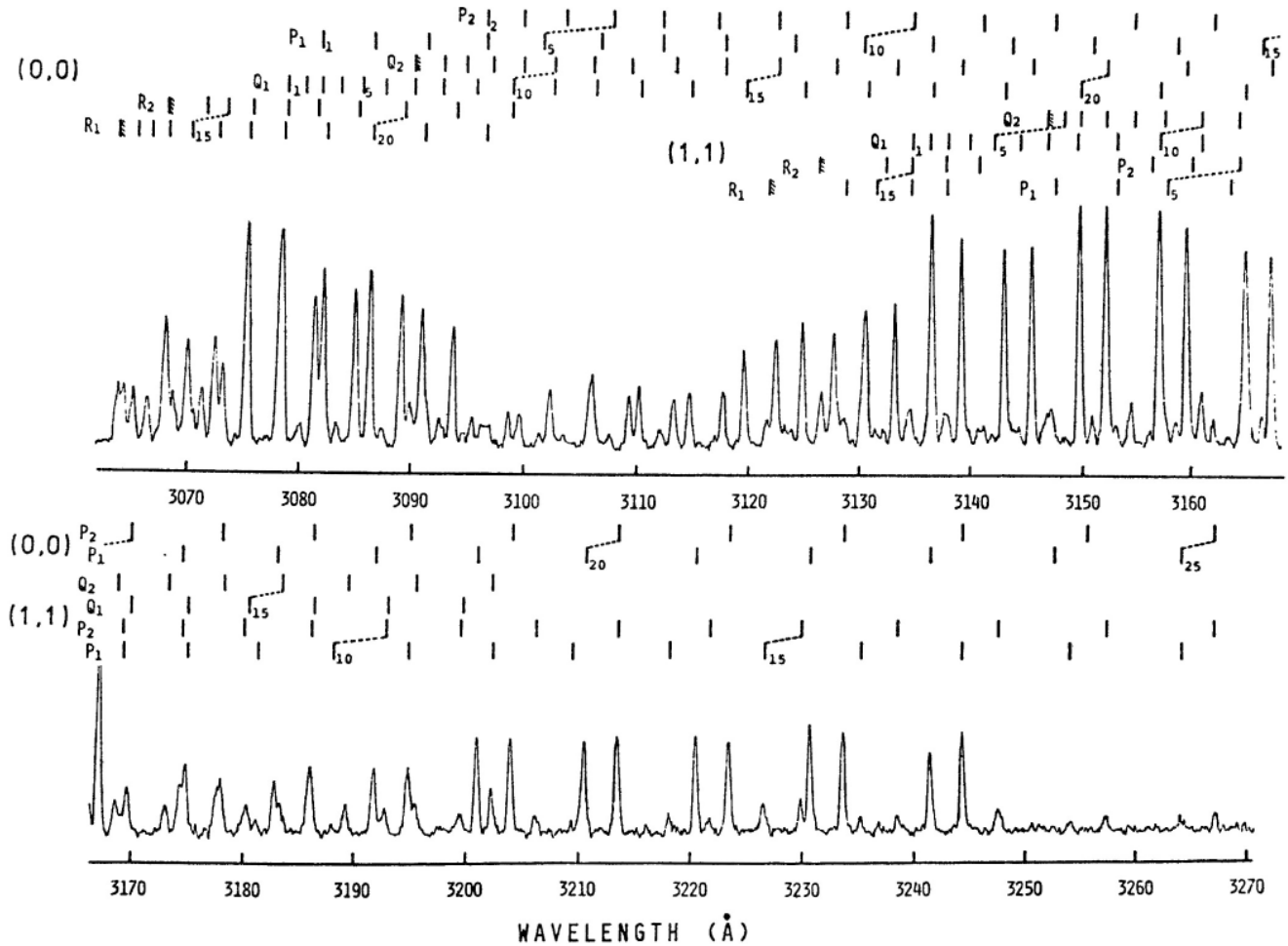

Fig. 5 A pen-recorder trace of the $A\ ^2\Sigma^+ \mathrm{A} \longrightarrow X\ ^2\Pi$ band-system of OH resulting from the Lyman α photon impact on H_2O in the crossed-beam experiment. The (0,0) band is dominant, and the weak (1,1) band is also recognized. Each band is consist of the six main branches designated by P_1, P_2, Q_1, Q_2, R_1 and R_2, whose band-heads are indicated by the hatched-lines.

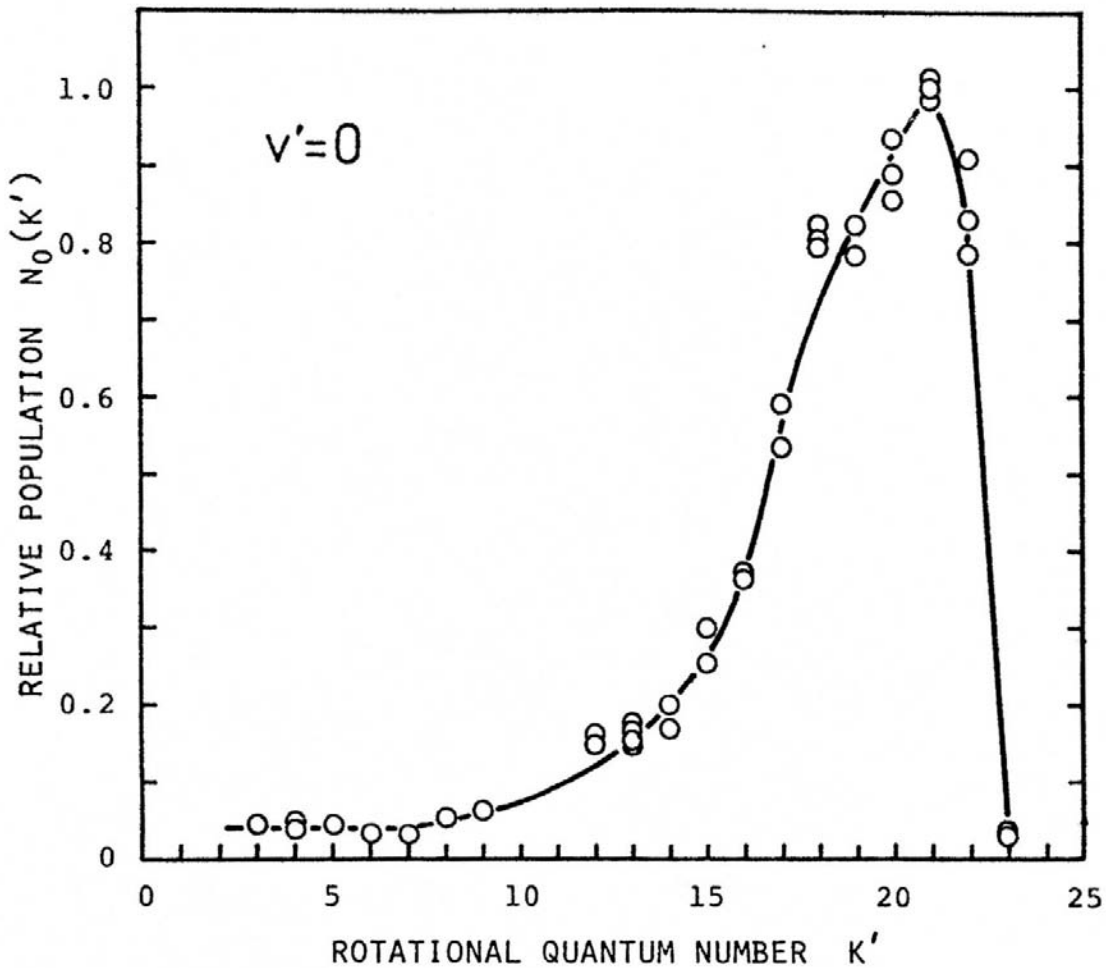

Fig.6 The rotational population distribution of OH($A\ ^2\Sigma^+$) for the vibrational state of $v' = 0$ obtained by the crossed-beam method. The population with the rotational quantum number K'; $N_0(K')$ is normalized so that the average population at $K' = 21$; $\langle N_0(21)\rangle$ is unity. The abrupt drop between $K' = 22$ and 23 corresponds to the energetical limit (see Fig.8).

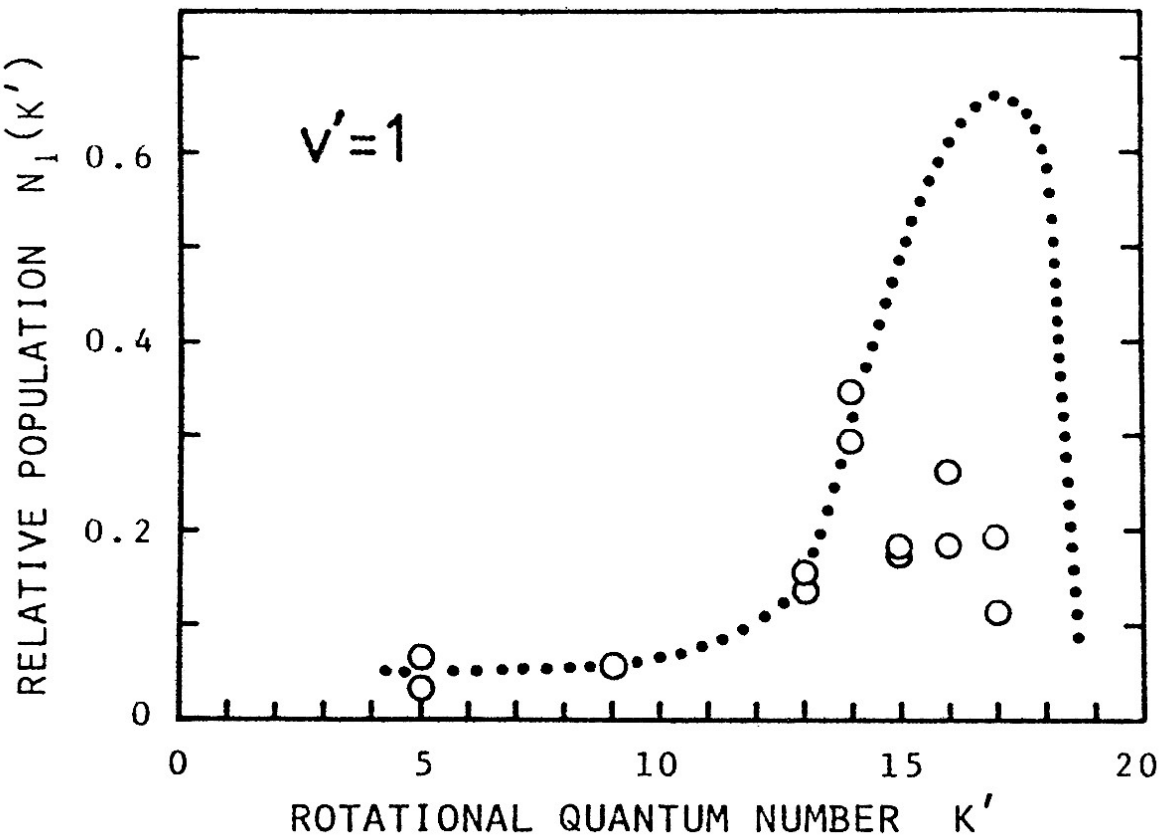

Fig. 7 The rotational population distribution of OH($A\ ^2\Sigma^+$) for the vibrational state of $v' = 1$ obtained by the crossed-beam method. The rotational population for $v' = 1$; $N_1(K')$ is normalized in the same way as in Fig.6, that is, $\langle N_0(21) \rangle = 1$.

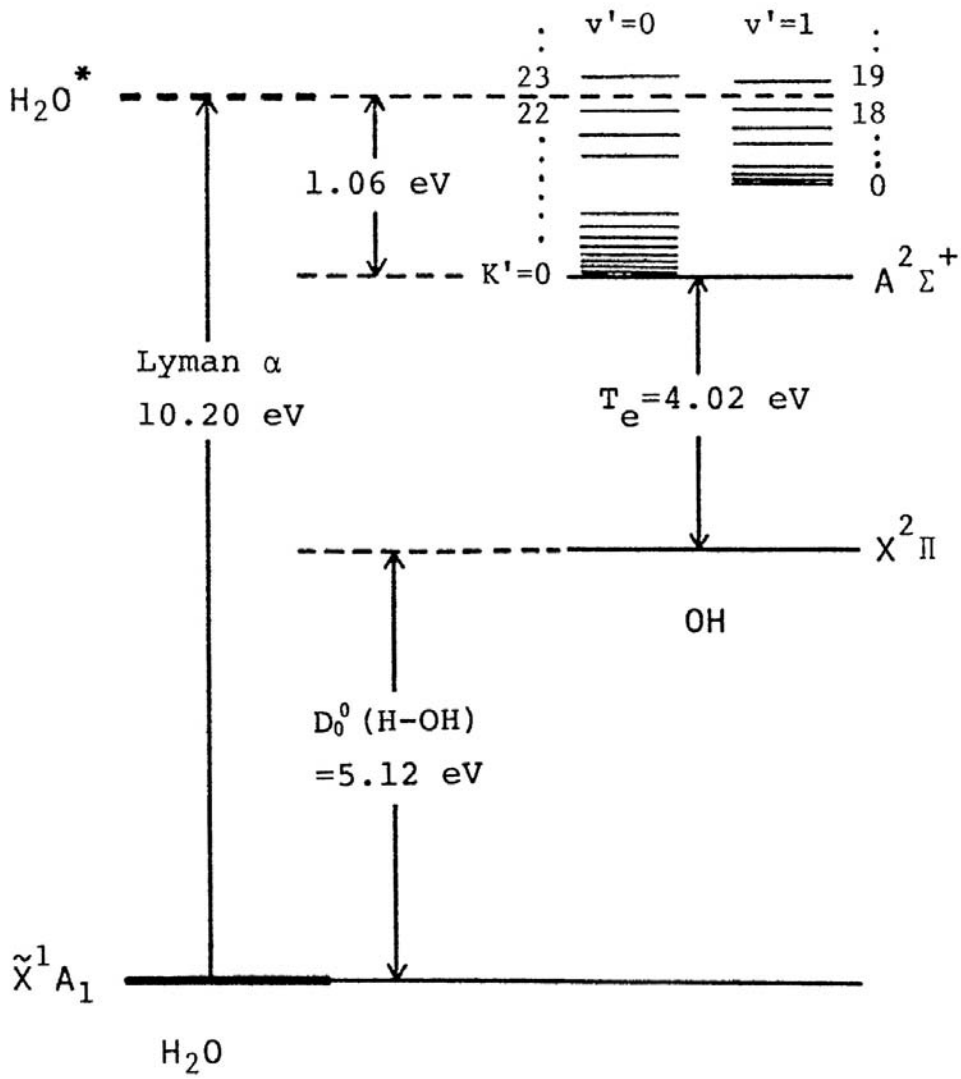

Fig.8 The energy level diagram related to the Lyman α photon-impact excitation of H_2O leading to OH($A\ ^2\Sigma^+$).

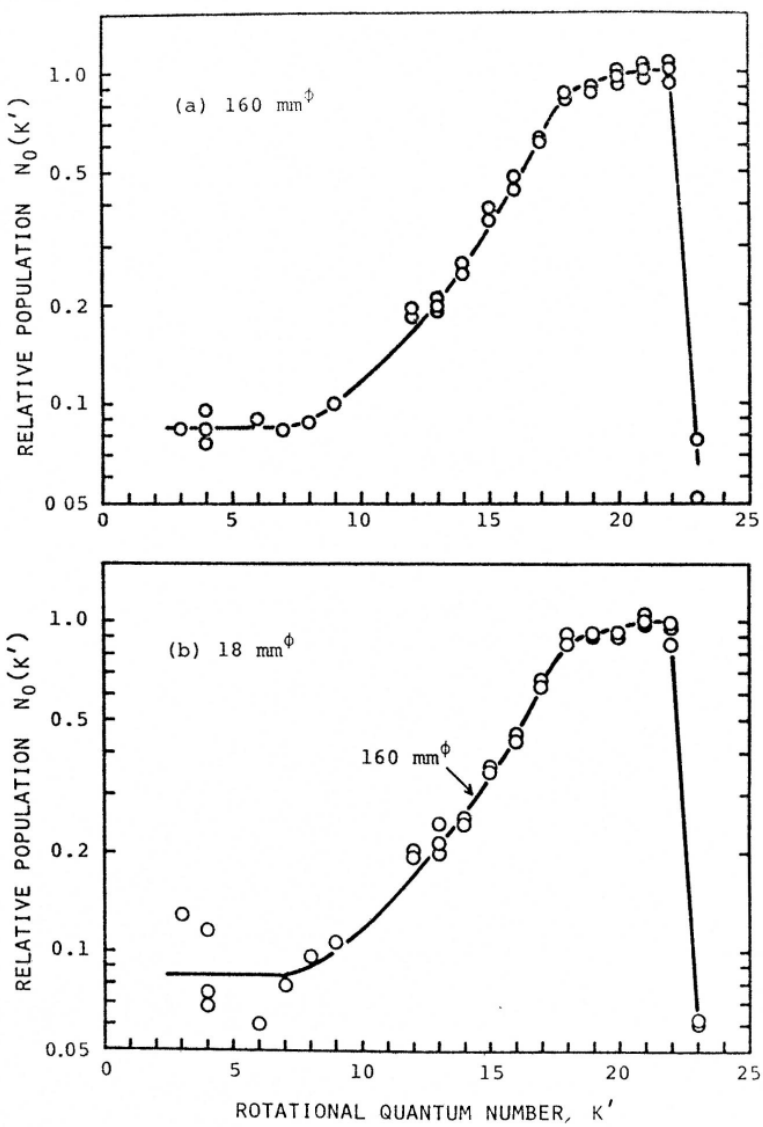

Fig.9 Comparison between the rotational distributions of OH($A\ ^2\Sigma^+$) for $v' = 0$ at the H_2O vapor pressure of 0.080 Torr in the fluorescence cells of the diameters of 160 and 18 mm obtained by the target-gas method. The population $N_0(K')$ is normalized so that $\langle N_0(21)\rangle = 1$.

(a) diameter 160 mm, (b) diameter 18 mm.

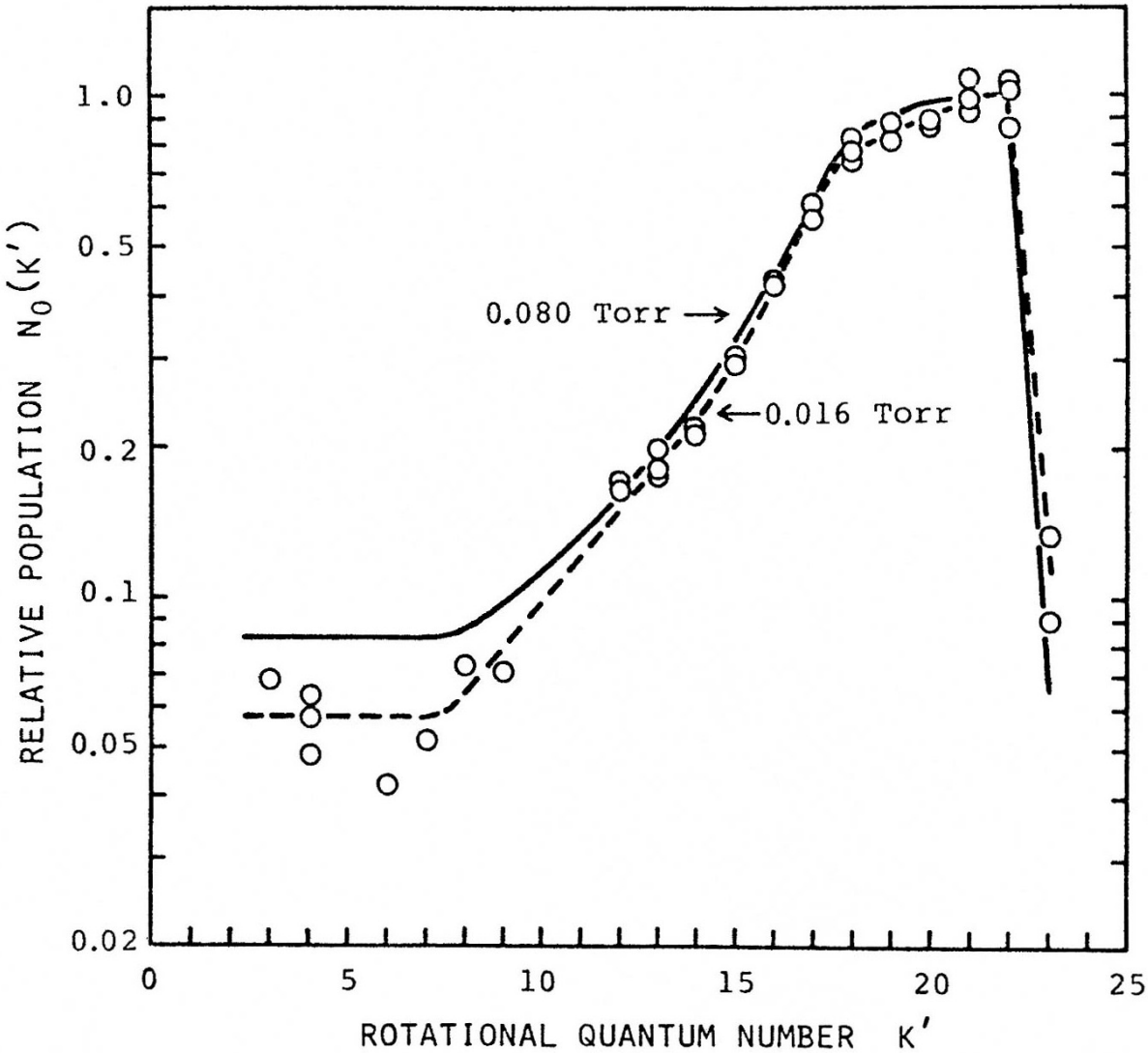

Fig.10 Comparison between the rotational distributions of OH($A\ ^2\Sigma^+$) for $v' = 0$ at the H_2O vapor pressures of 0.016 and 0.080 Torr in the fluorescence cell of 180 mm in diameter obtained by the target-gas method. The population $N_0(K')$ is normalized so that $\langle N_0(21)\rangle = 1$.

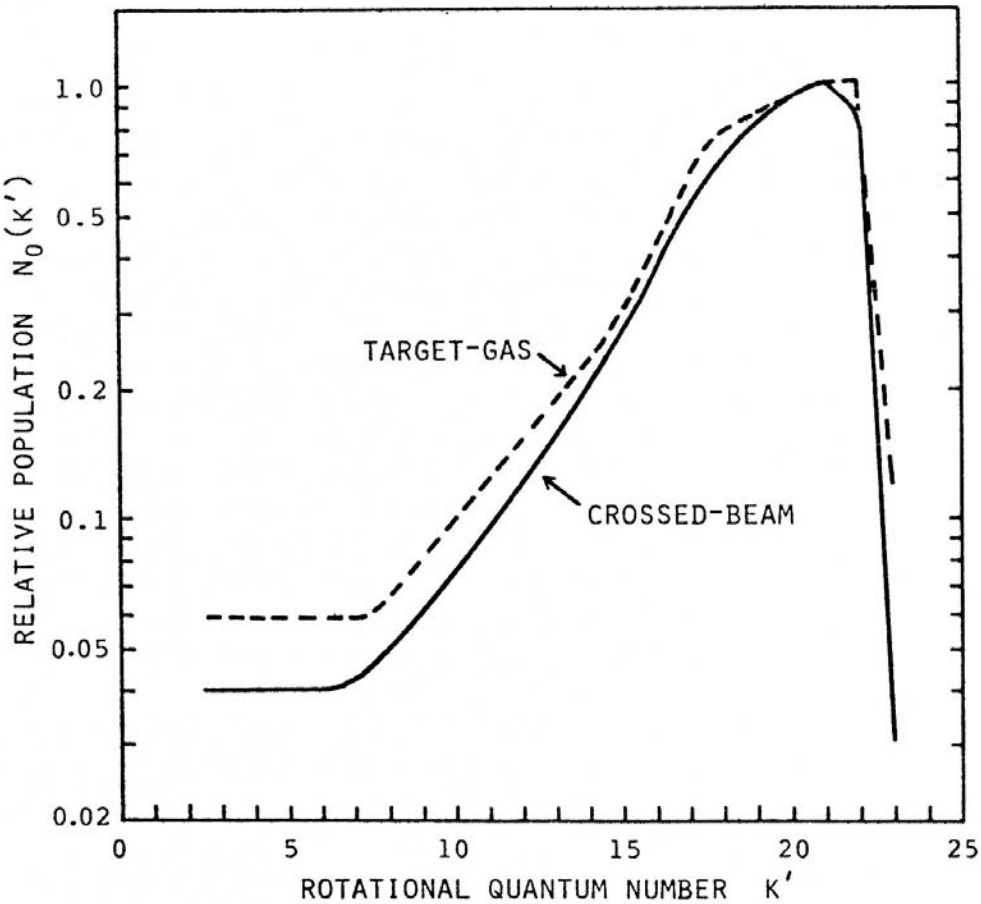

Fig.11 Comparison of the rotational distribution of OH($A\ ^2\Sigma^+$) for $v' = 0$ obtained by the target-gas method at the H_2O vapor pressure of 0.016 Torr with that by the crossed-beam method. The former is taken from Fig.10, and the latter is the same as Fig.6 except in the semi-logarithmic scale.

APPENDIX A

PREDISSOCIATION IN OH ($A\,^2\Sigma^+$)

As described in the section (3) of Part II, some anomalous decrease of populations appears in higher rotational levels ($K' \geq 15$) of $v' = 1$ state of OH($A\,^2\Sigma^+$). Such a phenomenon may be due to the predissociation of OH($A\,^2\Sigma^+$), which has so far been studied by many authors. As experimental results, the predissociation in OH($A\,^2\Sigma^+$) sets in not only at different rotational quantum numbers in different vibrational states, but also at different absolute energies. The predissociation probability is strongly dependent upon the rotational quantum number K', and according to Sutherland et al.[1)], the probability increases almost exponentially with K'. In addition, the F_1 spin component of the $A\,^2\Sigma^+$ state with $J'=K'+1/2$ is more strongly affected than the other spin component F_2 with $J'=K'-1/2$. According to Sutherland et al.[1)], the ratio of the predissociation probabilities of the F_1 and F_2 levels is 1.9 on the average.

In general, when a bound electronic state of a diatomic molecule is crossed by a repulsive state, the radiationless transition from the former to the latter is possible, and the predissociation to the separated atomic state takes place through the repulsive potential curve [2)]. In this case, there have been well-known selection rules, called the Kronig's rules for predissociation.

The Kronig's selection rules have been derived from the conditions for non-vanishing of the perturbation matrix elements between two states, which result from the terms neglected on the separation of the Schrödinger equation in the Born-Oppenheimer approximation [3]. They are expressed as follows [2].

(1) Both states must have the same total angular momentum J; that is, $\Delta J = 0$.

(2) Both states must have the same symmetry; that is, $+ \leftarrow/\rightarrow -$, and moreover $s \leftarrow/\rightarrow a$ for identical nuclei.

(3) Both states must have the same spin multiplicity; that is, $\Delta S = 0$.

(4) The resultant electronic angular momentum about the internuclear axis of the two states can differ only by 0 or ±1; that is, $\Delta \Lambda = 0, \pm 1$.

The first and second rules are perfectly rigorous. The fourth rule holds in Hund's cases (a) and (b).

A predissociation with $\Delta S \neq 0$ may occur, although this predissociation has only a small probability [2]. For such a "forbidden predissociation", the selection rule $\Delta S = \pm 1$ in Hund's cases (a) and (b) is given by Kovacs in consideration of the spin-orbit interaction [4].

Theoretically, the predissociation affecting the lower vibrational states of OH($A\ ^2\Sigma^+$) has been attributed to the radiationless transition

to the $^4\Sigma^-$ state arising from O(^3P) + H(^2S) [5,6]. The repulsive potential curve of $^4\Sigma^-$ state crosses the potential curve of $A\ ^2\Sigma^+$ on the outer limb of the latter one. However, the interaction between $^2\Sigma^+$ and $^4\Sigma^-$ violates the spin selection rule $\Delta S = 0$.

The predissociation probability in OH($A\ ^2\Sigma^+$) which is $\leq 10^7$ s^{-1} is quite small compared to the order of 10^{11}s^{-1} in a strong allowed predissociation[3], but still competes with the radiative transition probability[1] of about 10^6 s^{-1}.

In this way, the predissociation in OH($A\ ^2\Sigma^+$) is clearly of the forbidden nature. According to the selection rules, the nonzero perturbation between the $^2\Sigma^+$ and $^4\Sigma^-$ states occurs at the dotted intersections in Fig.1. This figure indicates the additional selection rule for the rotational quantum number K ; $\Delta K = \pm 1$.

The predissociation probability A_D is related to the perturbation matrix elements of the two interacting states. If the perturbation is separable into vibrational and electronic-rotational parts, the following relationship holds.

$$A_D = |H_{el\text{-}rot}|^2\ |H_{vib}|^2. \qquad (1)$$

The electronic and rotational part $|H_{el\text{-}rot}|^2$ for the $^2\Sigma^+$–$^4\Sigma^-$ interaction is given explicitly for Hund's case (b) coupling [4], which is dominant for Σ states, as follows;

$$\left.\begin{aligned} |H(F_1, F_3)|^2 &= \varepsilon\,[(K'+2)/(2K'+1)], \\ |H(F_2, F_4)|^2 &= \varepsilon\,[3(K'+1)/(2K'-1)], \\ |H(F_1, F_1)|^2 &= \varepsilon\,[3K'/(2K'-1)], \\ \text{and}\quad |H(F_2, F_2)|^2 &= \varepsilon\,[(K'-2)/(2K'-1)], \end{aligned}\right\} \tag{2}$$

where ε is an undetermined constant. These nonzero matrix elements correspond to the dotted intersections in Fig.l, respectively, and they are essentially independent of K'. Therefore, the observed dependence of the predissociation probability on the vibrational and rotational quantum numbers must be accounted for by means of the other term in the equation (1), that is, the vibrational part $|H_{vib}|^2$.

According to the equations (2), the predissociation in the F_1 level is stronger than in the F_2 level by a factor of 3 at the lower crossing points in Fig.1. On the other hand, for the interactions which correspond to the higher crossing points, the F_2 level is favored by a factor of 3. Therefore, the stronger predissociation of the F_1 levels observed by Sutherland et al. indicates that the crossings at lower energy are the more important [1)].

H_{vib} is essentially the overlap integral of the two vibrational eigenfunctions for the discrete state $A\ ^2\Sigma^+$ and the continuous state $^4\Sigma^-$. The overlap integral can be estimated qualitatively by sketching the relevant potential curves and vibrational eigenfunctions. Effective potential curves including the centrifugal potential due to rotation are

drawn in Fig.2 for different rotational quantum numbers; 0, 15, 22 and 30. The $A\,^2\Sigma^+$ potential curve of $K' = 0$ is the experimental curve obtained by Fallon et al.[7]. The $^4\Sigma^-$ potential curve of $K'' = 0$ is the theoretical curve calculated by Michels et al. [5].

After this, $\Delta K = 0$ is assumed for simplicity, although $\Delta K = \pm 1$ as mentioned before. In Fig.2, are drawn schematically the vibrational eigenfunctions for a discrete level ($v' = 1$ and $K' = 22$) and a continuous level ($K'' = 22$) having the same energy, where the energy levels lie in the neighborhood of the crossing point between the potential curves. The eigenfunctions lie in such a way with respect to each other that the overlap integral has a considerable magnitude, and therefore the predissociation will take place with a fairly large probability.

In the discrete level of $v' = 1$ and $K' = 15$, a potential barrier exists between the discrete and continuous levels. However, quantum-mechanically, the transition between the levels will take place with a certain probability due to "tunnel-effect", because the overlap of the eigenfunctions is not negligible. On the other hand, it is seen in the case of $v' = 0$ and $K' = 22$ that the overlap of the eigenfunctions is vanishingly small and moreover a considerably high potential barrier exists between the levels. Therefore, the predissociation is not expected. In the case of $v' = 2$, the predissociation is expected to set in at $K' = 0$.

In this manner, the dependence of the predissociation on v' and K' can be accounted for qualitatively. The quantitative calculation of the overlap integrals has been made recently by Smith et al.[8], but such a calculation is only tentative for lack of the detailed informations about the potential curves, especially of the $^4\Sigma^-$ state.

References

1) R.A. Sutherland and R.A. Anderson: J. chem. Phys. **58** (1973) 1226.
2) G. Herzberg: *Spectra of Diatomic Molecules* (D. Van Nostrand, New York, 1950).
3) R.L. Kronig: Z. Phys. **50** (1928) 347.
4) I. Kovacs: *Rotational Structure in the Spectra of Diatomic Molecules* (Adam Hilger, London, 1969).
5) H.H. Michels and F.E. Harris: Chem. Phys. Lett. **3** (1969) 441.
6) A.G. Gaydon and I. Kopp: J. Phys. **B4** (1971) 752.
7) R.J. Fallon, I. Tobias and J.T. Vanderslice: J. chem. Phys. **34** (1961) 167.
8) W.H. Smith, B.G. Elmergreen and N.H. Brooks: J. chem. Phys. **61** (1974) 2793.

Figure Captions

Fig. 1 Intersections of the potential curves of the $^2\Sigma^+$ and $^4\Sigma^-$ states in the Hund's case (b) coupling. The rotational state of $^2\Sigma^+$ with K' splits into the two terms; F_1 ($J'=K'+1/2$) and F_2 ($J'=K'-1/2$). The rotational state of $^4\Sigma^-$ with K'' splits into the four terms; F_1 ($J''=K''+3/2$), F_2 ($J''=K''+1/2$), F_3 ($J''=K''-1/2$) and F_4 ($J''=K''-3/2$) . The nonzero perturbation occurs at the dotted intersections, which lead to the additional selection rule for the predissociation; $\Delta K = \pm 1$.

Fig. 2 The effective potential curves of the $A\ ^2\Sigma^+$ and $^4\Sigma^-$ states of OH for the different rotational quantum numbers; 0, 15, 22 and 30. The horizontal lines indicate the vibrational-rotational levels of the discrete $A\ ^2\Sigma^+$ state. The broken-line curves are the vibrational eigenfunctions for the discrete level with $v' = 1$ and $K' = 22$ and for the continuous level of the $^4\Sigma^-$ state having the same energy and the same rotational quantum number (only qualitatively drawn).

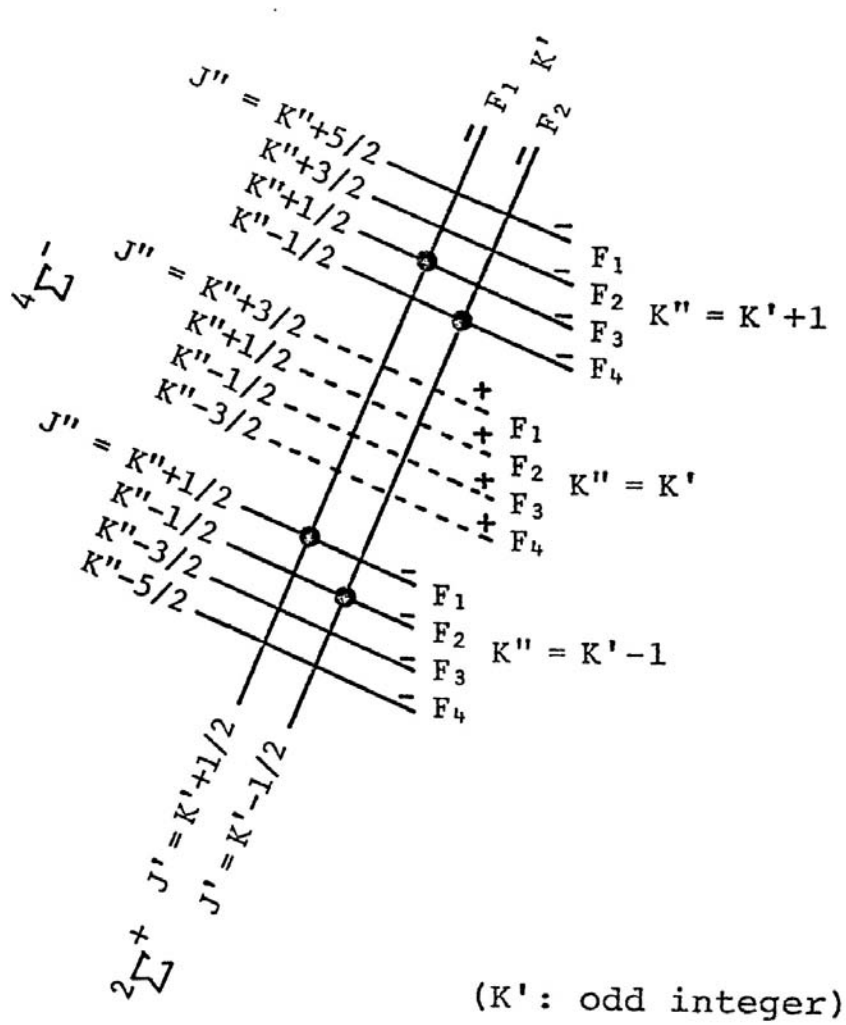

Fig. 1 Intersections of the potential curves of the $^2\Sigma^+$ and $^4\Sigma^-$ states in the Hund's case (b) coupling. The rotational state of $^2\Sigma^+$ with K' splits into the two terms; F_1 ($J'=K'+1/2$) and F_2 ($J'=K'-1/2$). The rotational state of $^4\Sigma^-$ with K'' splits into the four terms; F_1 ($J''=K''+3/2$), F_2 ($J''=K''+1/2$), F_3 ($J''=K''-1/2$) and F_4 ($J''=K''-3/2$) . The nonzero perturbation occurs at the dotted intersections, which lead to the additional selection rule for the predissociation; $\Delta K = \pm 1$.

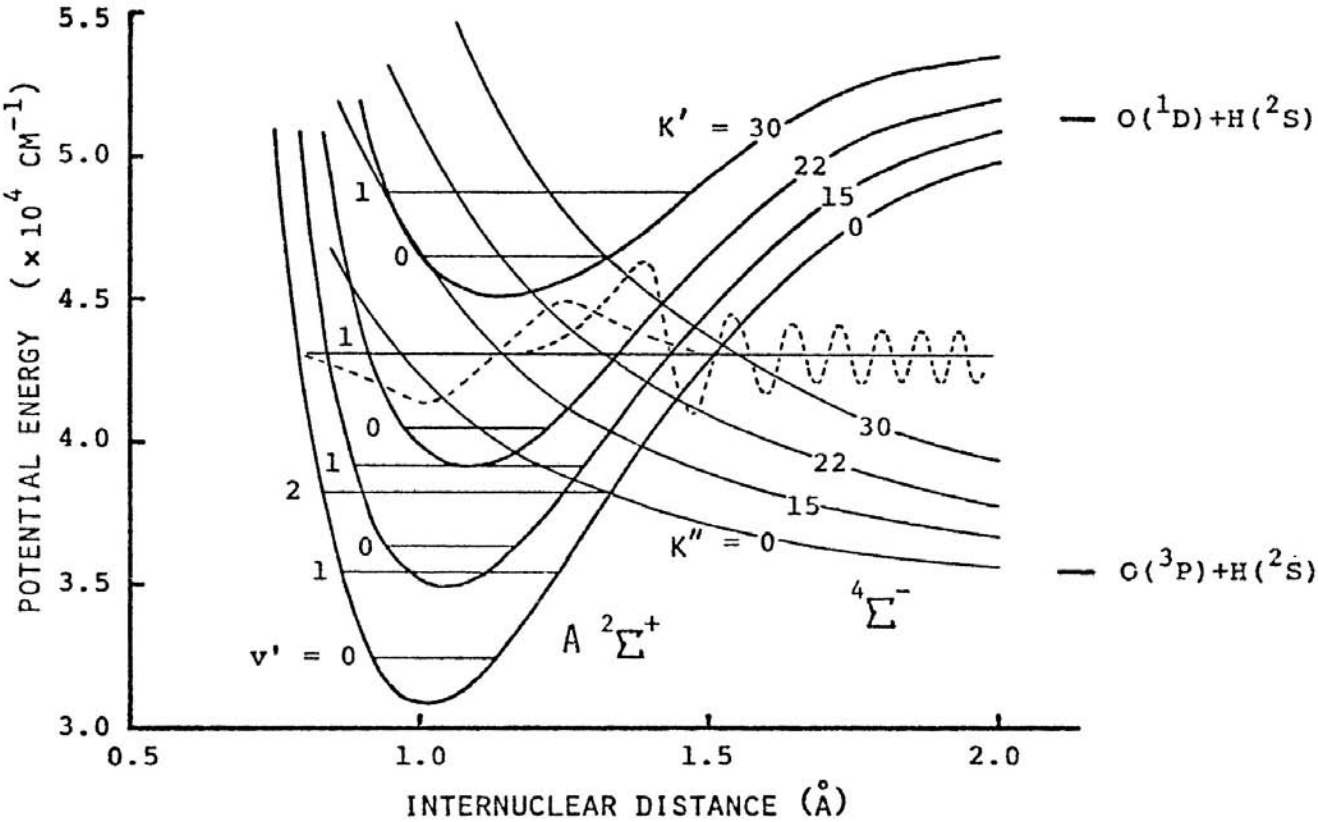

Fig. 2 The effective potential curves of the $A\ ^2\Sigma^+$ and $^4\Sigma^-$ states of OH for the different rotational quantum numbers; 0, 15, 22 and 30. The horizontal lines indicate the vibrational-rotational levels of the discrete $A\ ^2\Sigma^+$ state. The broken-line curves are the vibrational eigenfunctions for the discrete level with $v' = 1$ and $K' = 22$ and for the continuous level of the $^4\Sigma^-$ state having the same energy and the same rotational quantum number (only qualitatively drawn).

APPENDIX B

CORRELATION DIAGRAMS FOR ELECTRONIC STATES OF H_2O AND POTENTIAL ENERGY SURFACE OF THE $\widetilde{B}\ ^1A_1$ STATE

(1) Excited States of H_2O

The H_2O molecule in its ground state has the symmetry of C_{2v}, as shown in Fig.1(a). Its electron configuration is represented by

$$(1a_1)^2(2a_1)^2(1b_2)^2(3a_1)^2(1b_1)^2 \quad : \quad \widetilde{X}\ ^1A_1. \tag{1}$$

The lower excited states are obtained by exciting an electron from either the $1b_1$ or $3a_1$ orbital to the various higher Rydberg orbitals that arise from ns, np, nd,... atomic orbitals ($n \geq 3$). Because of the splitting of each degenerate atomic orbital, for example, there are three Rydberg series for np orbitals; that is, npa_1, npb_1 and npb_2. In Fig.2, the observed and calculated electronic states of H_2O are plotted in an energy level diagram, following Herzberg [1] and Goddard et al. [2]. The vertical position of each state corresponds to the vertical excitation energy in the equilibrium conformation of the ground state, which is shown in Fig.1(a).

(2) Correlation Diagrams

The correlations related to the following dissociations;

$$H_2O \longrightarrow O + H_2, \tag{2}$$

and $$H_2O \longrightarrow OH + H, \tag{3}$$

will be examined on the basis of the symmetry properties, where the necessary knowledge can be taken from the text by Herzberg [1]. The dissociations (2) and (3) may be treated in the symmetries of C_{2v} and C_s, respectively, as shown in Figs.1(b) and (c). In regard to such dissociations, the correlations have been studied by many authors [2-5]. This section is mainly dependent on the recent work by Tsurubuchi [6].

The O + H_2 system builds up the following electronic states of H_2O in the symmetry of C_{2v}.

$$\left.\begin{array}{l}
O(^3P_g) + H_2\ (X\ ^1\Sigma_g{}^+) \longrightarrow\ ^3A_2 + {}^3B_1 + {}^3B_2, \\
O(^1D_g) + H_2\ (X\ ^1\Sigma_g{}^+) \longrightarrow\ 2\,^1A_1 + {}^1A_2 + {}^1B_1 + {}^1B_2, \\
O(^1S_g) + H_2\ (X\ ^1\Sigma_g{}^+) \longrightarrow\ ^1A_1, \\
O(^3S_u) + H_2\ (X\ ^1\Sigma_g{}^+) \longrightarrow\ ^3A_2, \\
O(^3P_g) + H_2\ (b\ ^3\Sigma_u{}^+) \longrightarrow\ ^{1,3,5}A_1 + {}^{1,3,5}A_2 + {}^{1,3,5}B_1,
\end{array}\right\} \quad (4)$$

and so on.

The OH + H system correlates to the electronic states of H_2O in the symmetry of C_s, as follows;

$$\left.\begin{array}{l}
OH(X\ ^2\Pi) + H(^2S) \longrightarrow\ ^{1,3}A' + {}^{1,3}A', \\
OH(A\ ^2\Sigma^+) + H(^2S) \longrightarrow\ ^{1,3}A', \\
OH(^4\Sigma^-) + H(^2S) \longrightarrow\ ^{3,5}A'', \\
OH(^2\Sigma^-) + H(^2S) \longrightarrow\ ^{1,3}A'', \\
OH(^2\Delta) + H(^2S) \longrightarrow\ ^{1,3}A' + {}^{1,3}A'',
\end{array}\right\} \quad (5)$$

and so on. On the other hand, the electronic states of H_2O with the

symmetry of C_{2v} change their representations in the symmetry of C_s, as follows;

$$\left.\begin{array}{ll} A_1\ ,\ B_2 & \longrightarrow\ A', \\ \text{and}\quad A_2\ ,\ B_1 & \longrightarrow\ A''. \end{array}\right\} \qquad (6)$$

The assignments of the electronic states of H_2O and their order are presented in the energy level diagram of Fig.2. The electronic states of the fragment species; O, H and H_2 are well-known, and those of OH have been studied experimentally[7,8] and theoretically[9,10]. In addition, the dissociation energy of H_2O in the ground state is known as 5.12 eV for OH($X\ ^2\Pi$) + H(^2S) [1], which leads to the dissociation energy of 4.98 eV for O(^3P) + H_2 (X $^1\Sigma_g{}^+$).

As a result, the correlations for the dissociations (2) and (3) can be derived according to the non-crossing rule[1]. The correlation diagrams for singlet and triplet states of H_2O are shown in Figs.3 and 4, respectively. In the figures, a dotted horizontal line indicates such a dissociated system that contains an anti-bonding state of OH or H_2, and its vertical position corresponds to a relevant fully-dissociated system; H + H + O.

(3) Potential Energy Surface of the $\widetilde{B}\ ^1A_1$ state

In the case of photon-impact, the $\widetilde{X}\ ^1A_1$ ground state of H_2O can be excited only to some of the singlet excited states; $^1A_1$, $^1B_1$ and $^1B_2$, because of the spin selection rule of $\Delta S = 0$ and the requirement for the symmetry properties of the excited and ground states. The singlet state

which correlates to OH($A\ ^2\Sigma^+$) is only the $\widetilde{B}\ ^1A_1$ state of H_2O at 9.7 eV, as shown in Fig.3. In what follows, we will discuss the basic nature of the $\widetilde{B}\ ^1A_1$ state and refer to the theoretical potential energy surfaces obtained by several authors[11–13],

Some lower-lying singlet states concerned have the following electron configurations;

$$\left.\begin{array}{lll} \cdots\cdots\cdots\ (3a_1)^2\,(1b_1)^2 & : & \widetilde{X}\ ^1A_1\,, \\ \cdots\cdots\cdots\ (3a_1)^2\,(1b_1)\,(4a_1) & : & \widetilde{A}\ ^1B_1\,, \\ \cdots\cdots\cdots\ (3a_1)^2\,(1b_1)\,(2b_2) & : & ^1A_2\,, \\ \cdots\cdots\cdots\ (3a_1)\ (1b_1)^2\,(4a_1) & : & \widetilde{B}\ ^1A_1\,, \\ \text{and}\quad \cdots\cdots\cdots\ (3a_1)\ (1b_1)^2\,(2b_2) & : & ^1B_2\,, \end{array}\right\} \qquad (7)$$

where the $4a_1$ and $2b_2$ orbitals are equivalent to the $3sa_1$ and $3pb_2$ orbitals, respectively.

Considerations of LCAO-MO suggest that the $3a_1$ orbital is bonding, the $1b_1$ orbital non-bonding, and the $4a_1$ and $2b_2$ orbitals anti-bonding[1]. The variations of orbital energies in going from a bent (bond angle ∠HOH = 60°) to a linear conformation (∠HOH = 180°) are shown in the so-called Walsh diagram of Fig. 5 [12].

According to the Walsh diagram, the $3a_1$ orbital favors a bent conformation, while the $4a_1$ orbital favors the linear conformation. Then, $\widetilde{B}\ ^1A_1$ state may be most stable in the linear conformation. Besides, the $\widetilde{B}\ ^1A_1$ state will be unstable, because the $3a_1$ and $4a_1$ orbitalsare bonding

and anti-bonding, respectively. Therefore, the H_2O molecule excited from $\widetilde{X}\ ^1A_1$ to $\widetilde{B}\ ^1A_1$ is expected to split into certain fragments, while opening its bond angle largely.

The correlation diagrams between H_2O and OH + H in the symmetry of C_s have been presented in Figs.3 and 4. On the other hand, in the linear conformation with the $C_{\infty v}$ symmetry, the correlations must be re-examined as follows.

The singlet electronic states of H_2O take the following representations and electron configurations in the symmetry of $D_{\infty h}$ shown in Fig.1 (d);

$$\left.\begin{array}{lll} \widetilde{X}\ ^1A_1 & \longrightarrow & (1\sigma_g)^2\,(2\sigma_g)^2\,(1\sigma_u)^2\,(1\pi_u)^4 \quad : {}^1\Sigma_g{}^+ , \\ \widetilde{A}\ ^1B_1 \quad \widetilde{B}\ ^1A_1 & \longrightarrow & \cdots\cdots\cdots\cdots\ (1\pi_u)^3\,(3\sigma_g) \quad : {}^1\Pi_u , \\ {}^1A_2 ,\ {}^1B_2 & \longrightarrow & \cdots\cdots\cdots\cdots\ (1\pi_u)^3\,(2\sigma_u) \quad : {}^1\Pi_g , \end{array}\right\} \quad (8)$$

and so on, where the correspondence of a C_{2v} orbital to a $D_{\infty h}$ orbital is presented in Fig.5. Using the Walsh diagram of Fig.5, the dependence of energy upon the bond angle ∠HOH can be schematically drawn for some singlet states, as shown in Fig.6(a).

The OH + H system builds up the following electronic states of H_2O in the symmetry of $C_{\infty v}$;

$$\left.\begin{array}{lll} \mathrm{OH}(X\ ^2\Pi) + \mathrm{H}(^2S) & \longrightarrow & {}^{1,3}\Pi , \\ \mathrm{OH}(A\ ^2\Sigma^+) + \mathrm{H}(^2S) & \longrightarrow & {}^{1,3}\Sigma^+ , \end{array}\right\} \quad (9)$$

and so on. Then, the correlations in the linear conformation can be derived, as shown on the right side of Fig.6(a). The $\widetilde{X}\ ^1A_1$ and $\widetilde{B}\ ^1A_1$

states correlate to OH($A\ ^2\Sigma^+$) + H(^2S) and OH ($X\ ^2\Pi$) + H(^2S), respectively, where the potential crossing is allowed.

However, the crossing must be avoided in the bent conformation with the C_s symmetry, as shown in Fig.3, because both the $\widetilde{X}\ ^1A_1$ and $\widetilde{B}\ ^1A_1$ states become the same representation $^1A'$. In other words, the potential surfaces of the $\widetilde{X}\ ^1A_1$ and $\widetilde{B}\ ^1A_1$ states do intersect in the linear conformation, but repel each other in the bent conformation. Therefore, the cross-section of the $\widetilde{B}\ ^1A_1$ surface for a certain bond angle different from 180° will exhibit a minimum at a moderately large distance between H and OH, as shown in Fig.6(b). Such a situation is known as a "conical intersection" of two potential surfaces [1]. If the $\widetilde{B}\ ^1A_1$ state is most stable in the linear conformation as suggested above, the potential surface of the $\widetilde{B}\ ^1A_1$ state will exhibit a conical potential valley, whose apex corresponds to the crossing point in the linear conformation.

The potential surface of the $\widetilde{B}\ ^1A_1$ state has been theoretically calculated by Horsley et al.[11] and Claydon et al.[12]. However, their results do not possess such a basic nature as above mentioned, and also they have not brought any sufficient informations about the mechanism of the abnormal rotation of OH ($A\ ^2\Sigma^+$) split from H_2O by the Lyman α photon-impact.

Recently, the theoretical calculation consistent with the above considerations has been made by Flouquet et al.[13] in the "ab initio" LCAO-MO-SCF-CI method. Their result is drawn by means of contour lines in Fig.7. In this calculation, the internuclear distance of the remaining OH is fixed at the equilibrium distance of the ground state of H_2O, because the latter is almost equivalent to the equilibrium internuclear distance of OH($A\ ^2\Sigma^+$). As expected, this potential surface possesses the conical potential valley, whose apex lies at the distance between H and OH of about 1.5 Å in the linear conformation. This surface is probably appropriate to account for the abnormal rotation of OH($A\ ^2\Sigma^+$), as discussed in the section (4) of Part II. In addition, this surface suggests that discrete vibrational states may exist even in the Franck-Condon region. This fact may account for the long progression bands extending from λ 1411 to 1256 with the spacing of about 800 cm^{-1} observed in the absorption spectrum[14], which is ascribed by Herzberg[1] to the bending vibration of $H_2O(\widetilde{B}\ ^1A_1)$.

As a result, the conical intersection dominates the potential energy surface of the $\widetilde{B}\ ^1A_1$ state for the dissociation into OH($A\ ^2\Sigma^+$) + H(^2S).

References

1) G. Herzberg: *Electronic Spectra and Electronic Structure of Polyatomic Molecules* (D. Van Nostrand, New York, 1966).
2) W.A. Goddard III and W.J. Hunt: Chem. Phys. Lett. **24** (1974) 464.
3) K.E. Shuler: J. chem. Phys. **21** (1953) 624.
4) K.J. Laidler: J. chem. Phys. **22** (1954) 1740.
5) F. Fiquet-Fayard: J. chim. Phys. **57** (1960) 453.
6) S. Tsurubuchi: J. Phys. Soc. Japan (to be published).
7) R.J. Fallon, I. Tobias and J.T. Vanderslice: J. chem. Phys. **34** (1961) 167.
8) C. Carlone and F.W. Dalby: Can. J. Phys. **47** (1968) 1945.
9) H.H. Michels and F.E. Harris: Chem. Phys. Lett. **3** (1969) 441.
10) I. Easson and M.H.L. Pryce: Can. J. Phys. **51** (1973) 518.
11) J.A. Horsley and W.H. Fink: J. chem. Phys. **50** (1969) 750.
12) C.R. Claydon, G.A. Segal and H.S. Taylor: J. chem. Phys. **54** (1971) 39.
13) F. Flouquet and J.A. Horsley: J. chem. Phys. **60** (1974) 3767.
14) K. Watanabe and M. Zelikoff: J. Opt. Soc. Amer. **43** (1953) 753.

Figure Captions

Fig.1 Various conformations of H_2O and their symmetries.

(a) The equilibrium conformation of the $\widetilde{X}\ ^1A_1$ ground state with the symmetry of C_{2v}.

(b) The conformation for the dissociation O + H_2 in the symmetry of C_{2v}.

(c) The conformation for the dissociation OH + H in the symmetry of C_s.

(d) The linear conformations with the symmetries of $C_{\infty v}$ and $D_{\infty h}$

Fig. 2 Energy level diagram for the electronic states of H_2O in the equilibrium conformation of the $\widetilde{X}\ ^1A_1$ ground state. These states belong to the Rydberg series obtained by exciting an electron from either the $1b_1$ or $3a_1$ orbital to various higher orbitals. The states indicated by the dashed-lines have not been observed and their positions are drawn according to the theoretical calculation [2)].

Fig.3 Correlation diagram for the singlet states of H_2O and fragment species. H_2O correlates to the O + H_2 and OH + H systems in the symmetries of C_{2v} and C_s, respectively. Along the central axis, some singlet states of H_2O are indicated at the positions of their vertical energies given in Fig.2.

Fig.4 Correlation diagram for the triplet states of H_2O and fragment species. H_2O correlates to the O + H_2 and OH + H systems in the symmetries of C_{2v} and C_s, respectively. Along the central axis, some triplet states of H_2O are indicated at the positions of their vertical energies given in Fig.2.

Fig.5 Walsh diagram for the molecular orbitals of H_2O [12]. The variation of orbital energies in going from a bent (∠HOH = 60°) to a linear conformation (∠HOH = 180°) is shown, where the internuclear distance is fixed at the equilibrium distance (see Fig.1(a)). The correlations between the orbitals with the symmetries of C_{2v} (bent) and $D_{\infty h}$ (linear) are also shown. The $4a_1$ and $2b_2$ orbitals are identical with the $3sa_1$ and $3pb_2$ orbitals in Fig.2, respectively, and they are unoccupied in the $\widetilde{X}\ ^1A_1$ ground state.

Fig.6 The correlation diagrams predicting the potential energy surface of H_2O ($\widetilde{B}\ ^1A_1$) for the dissociation OH ($A\ ^2\Sigma^+$) + H (^2S) .

(a) The correlation in the linear conformation (∠HOH = 180°) with the symmetry of $C_{\infty v}$ shown in Fig. 1 (d).

(b) The correlation in the bent conformation with the symmetry of C_s shown in Fig.1 (c).

The left-hand side of each figure shows such a dependence of energy upon the bond angle ∠HOH that is expected from the

molecular orbital consideration. The potential energy surface of the $\widetilde{B}\ ^1A_1$ state is expected to possess a conical valley, whose apex lies a moderately large distance between H and OH in the linear conformation.

Fig.7 The contour map of the theoretical potential energy surface of H_2O ($\widetilde{B}\ ^1A_1$) for the dissociation OH($A\ ^2\Sigma^+$) + H(^2S) obtained by Flouquet et al. [13]. The contour interval is 0.27 eV. This surface exhibits such a conical potential valley as predicted in Fig. 6.

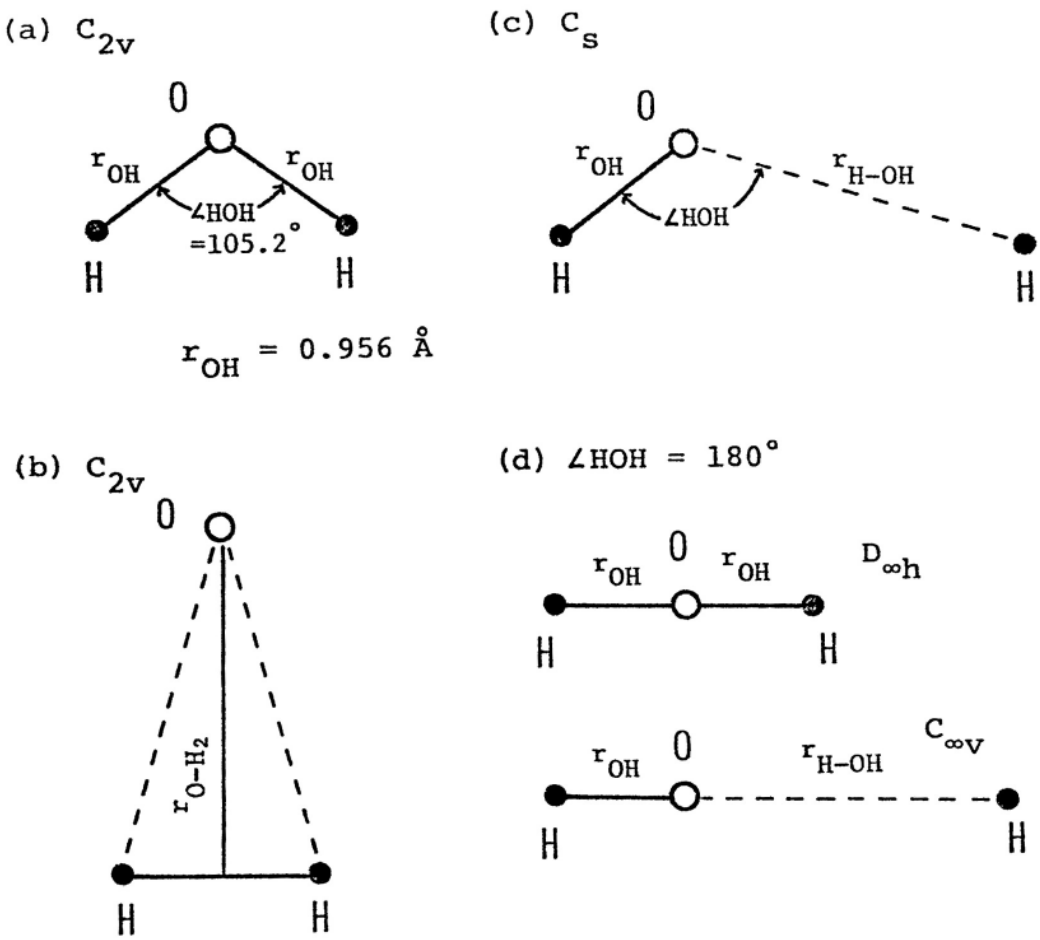

Fig.1 Various conformations of H_2O and their symmetries.

(a) The equilibrium conformation of the $\widetilde{X}\ ^1A_1$ ground state with the symmetry of C_{2v}.

(b) The conformation for the dissociation O + H_2 in the symmetry of C_{2v}.

(c) The conformation for the dissociation OH + H in the symmetry of C_s.

(d) The linear conformations with the symmetries of $C_{\infty v}$ and $D_{\infty h}$

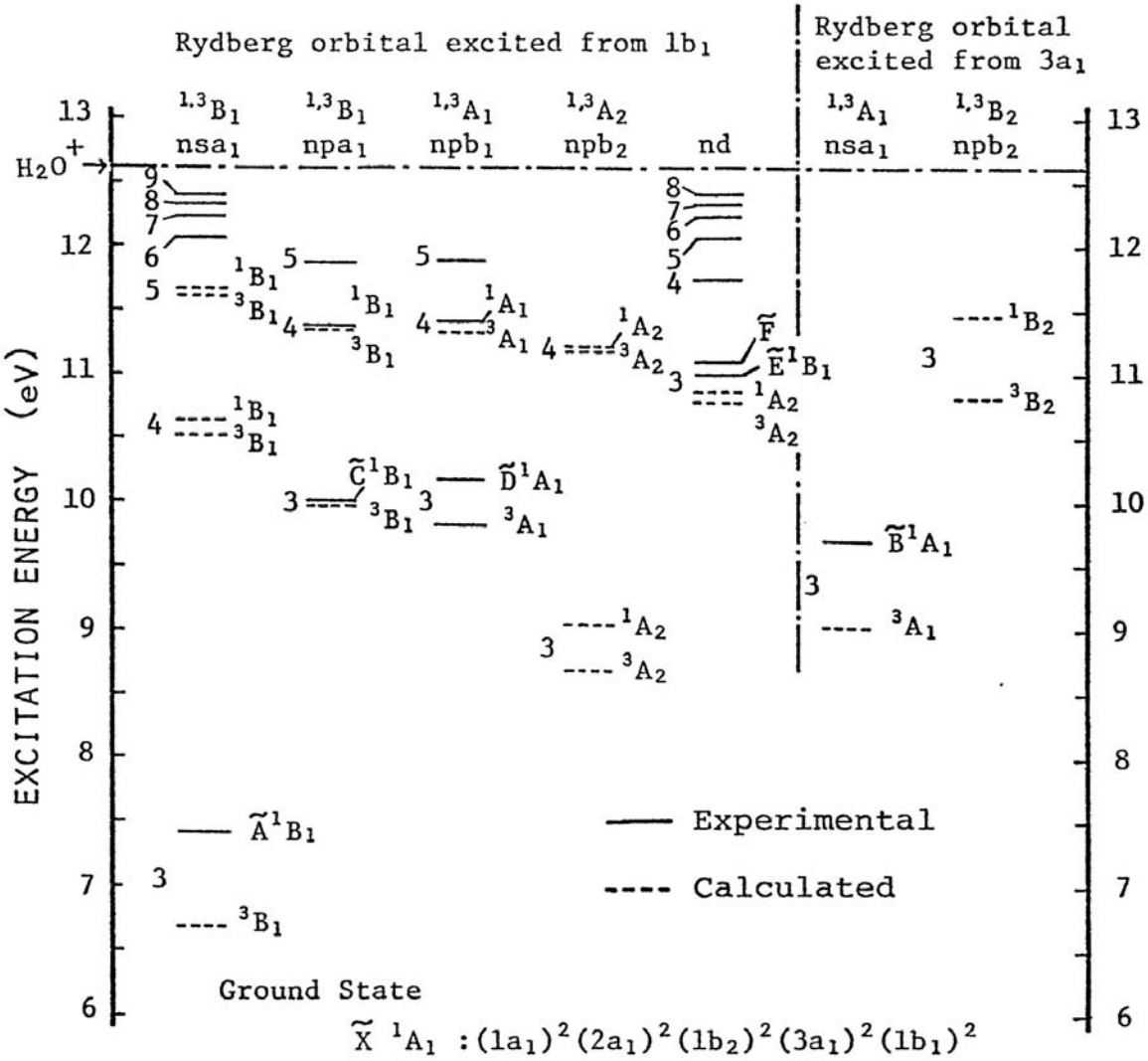

Fig. 2 Energy level diagram for the electronic states of H_2O in the equilibrium conformation of the $\widetilde{X}\ ^1A_1$ ground state. These states belong to the Rydberg series obtained by exciting an electron from either the $1b_1$ or $3a_1$ orbital to various higher orbitals. The states indicated by the dashed-lines have not been observed and their positions are drawn according to the theoretical calculation [2].

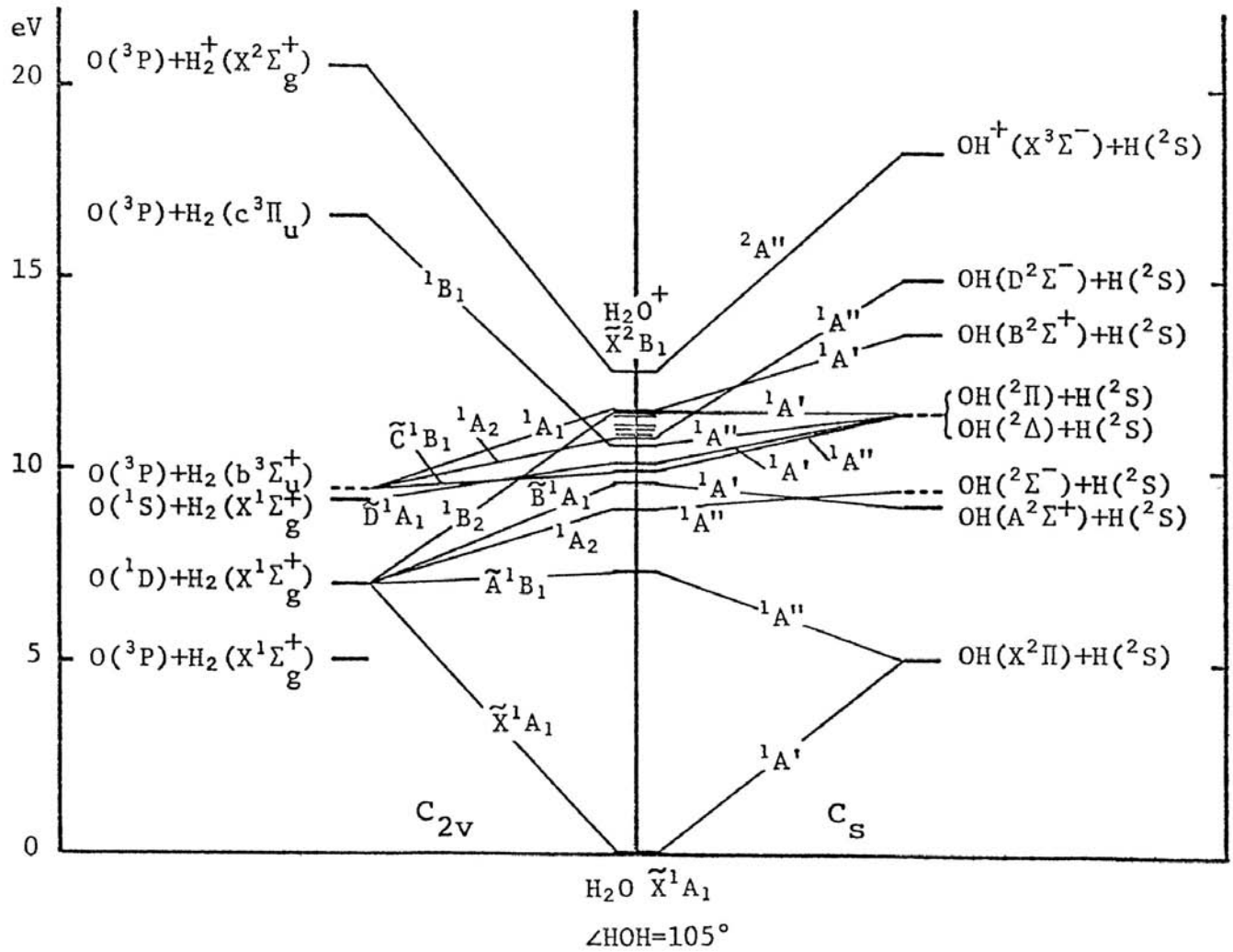

Fig.3 Correlation diagram for the singlet states of H_2O and fragment species. H_2O correlates to the O + H_2 and OH + H systems in the symmetries of C_{2v} and C_s, respectively. Along the central axis, some singlet states of H_2O are indicated at the positions of their vertical energies given in Fig.2.

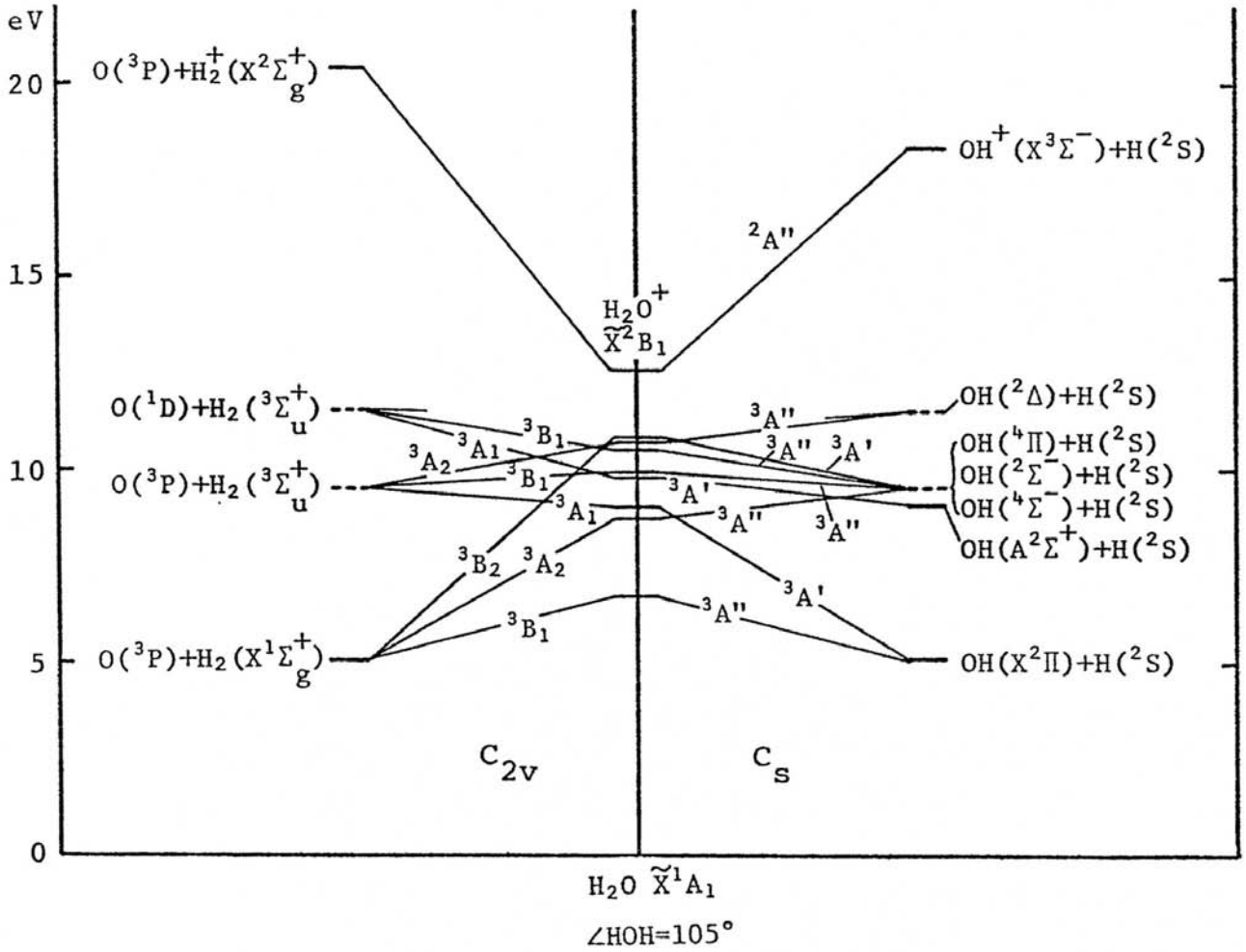

Fig.4 Correlation diagram for the triplet states of H_2O and fragment species. H_2O correlates to the O + H_2 and OH + H systems in the symmetries of C_{2v} and C_s, respectively. Along the central axis, some triplet states of H_2O are indicated at the positions of their vertical energies given in Fig.2.

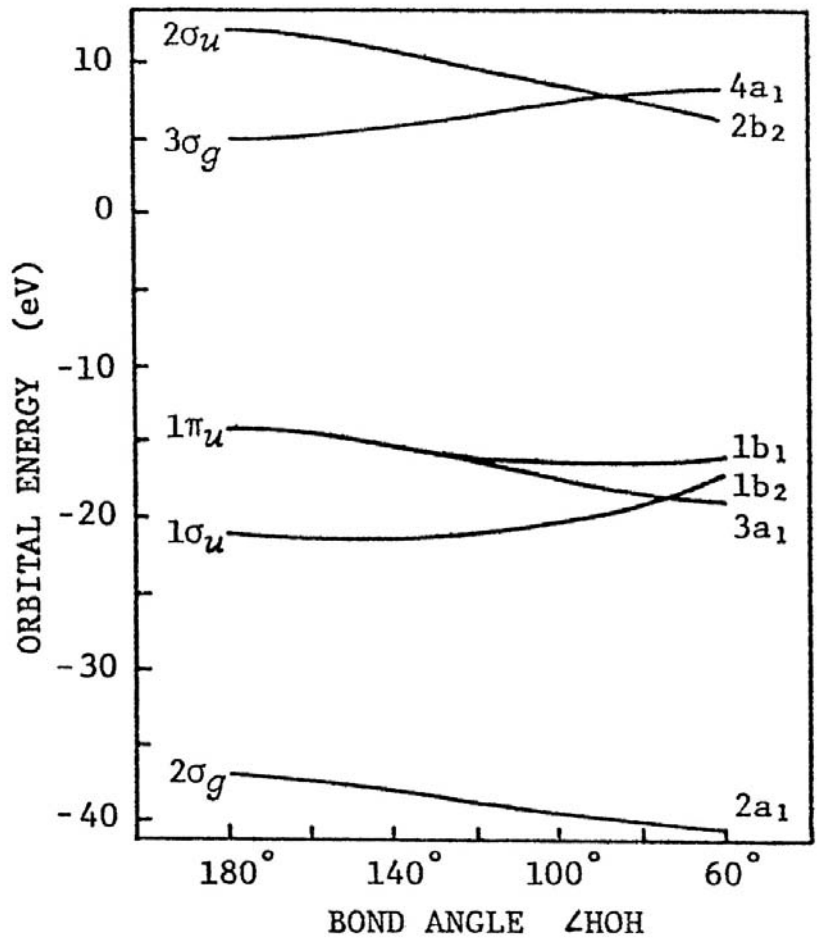

Fig.5 Walsh diagram for the molecular orbitals of H_2O [12]. The variation of orbital energies in going from a bent (∠HOH = 60°) to a linear conformation (∠HOH = 180°) is shown, where the internuclear distance is fixed at the equilibrium distance (see Fig.1(a)). The correlations between the orbitals with the symmetries of C_{2v} (bent) and $D_{\infty h}$ (linear) are also shown. The $4a_1$ and $2b_2$ orbitals are identical with the $3sa_1$ and $3pb_2$ orbitals in Fig.2, respectively, and they are unoccupied in the $\widetilde{X}\ ^1A_1$ ground state.

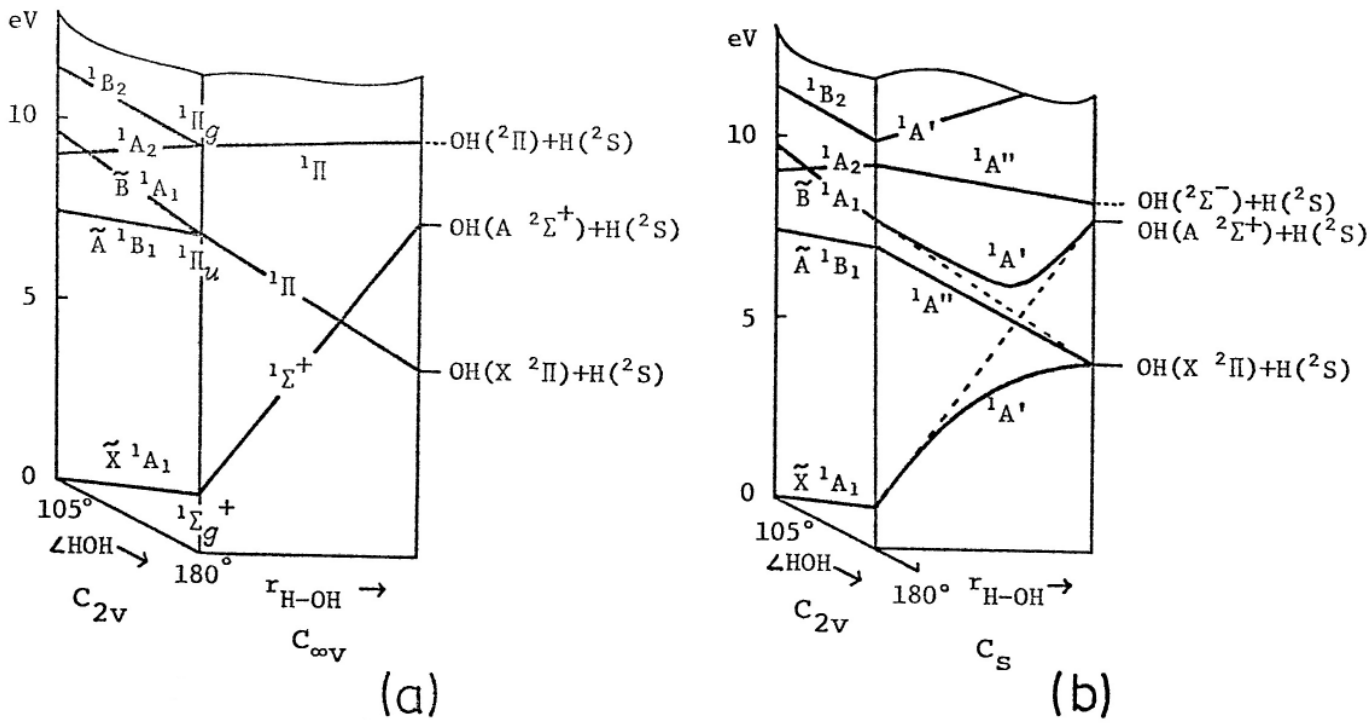

Fig.6 The correlation diagrams predicting the potential energy surface of $H_2O(\tilde{B}\ ^1A_1)$ for the dissociation OH ($A\ ^2\Sigma^+$) + H (^2S) .

(a) The correlation in the linear conformation (∠HOH = 180°) with the symmetry of $C_{\infty v}$ shown in Fig. 1 (d).

(b) The correlation in the bent conformation with the symmetry of C_s shown in Fig.1 (c).

The left-hand side of each figure shows such a dependence of energy upon the bond angle ∠HOH that is expected from the molecular orbital consideration. The potential energy surface of the $\tilde{B}\ ^1A_1$ state is expected to possess a conical valley, whose apex lies a moderately large distance between H and OH in the linear conformation.

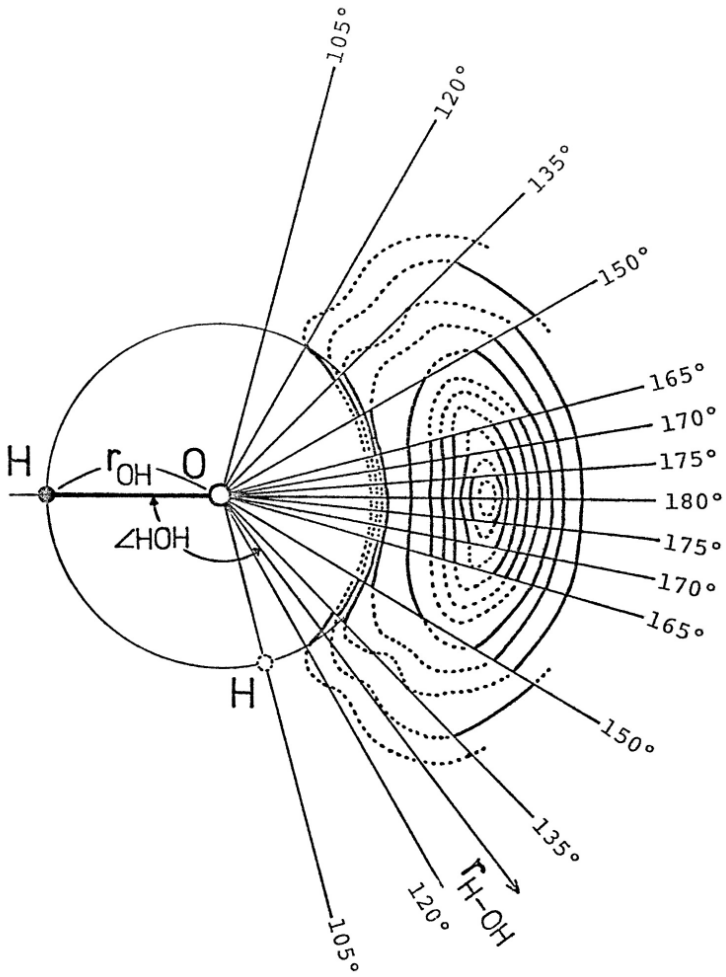

Fig.7 The contour map of the theoretical potential energy surface of $H_2O(\widetilde{B}\ ^1A_1)$ for the dissociation $OH(A\ ^2\Sigma^+) + H(^2S)$ obtained by Flouquet et al. [13]. The contour interval is 0.27 eV. This surface exhibits such a conical potential valley as predicted in Fig. 6.

Acknowledgements

This work has been undertaken by the present author during his stay in the graduate course of Osaka University, and continued after his removal to the Mechanical Engineering Laboratory. From beginning of the instrumentation to settlement of the manuscript, the author has long been very much obliged to Professor Tadao Horie, to whom the author would like to express his gratitude from the bottom of his heart. He would like to express his thanks to Associate Professor Tsuruji Iwai, Dr. Seiji Tsurubuchi, and Dr. Masahiro Kimura for their helpful advices and invaluable suggestions.

The author would like to thank to the many members of his laboratory; Director-General Masao Kubota, Vice Director-General Joji Yamaga, Head of Basic Engineering Division Naohisa Teshirogi, and Chief of Energy Section Tetsuo Yamanishi for their encouragements and giving a chance to continue this work.